

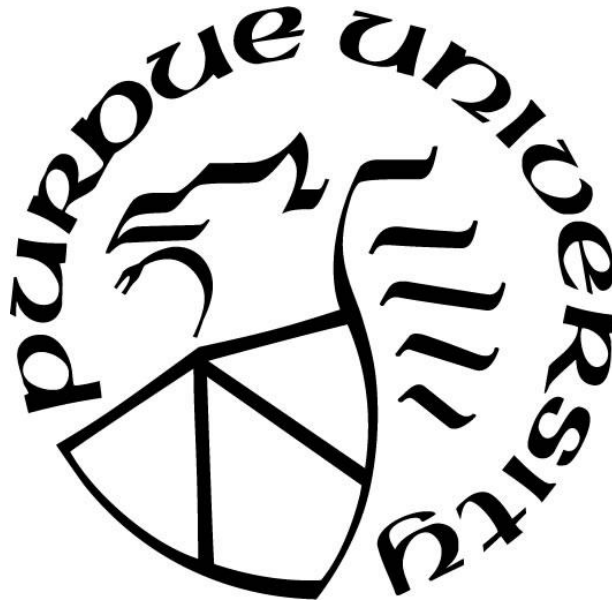
# **MULTI-FIDELITY ML BASED APPROACH TO PREDICT LOCAL MATERIAL RESPONSE**

by  
**Ayush Rai**

**A Thesis**

*Submitted to the Faculty of Purdue University  
In Partial Fulfillment of the Requirements for the degree of*

**Master of Science in Aeronautics and Astronautics**



School of Aeronautics and Astronautics

West Lafayette, Indiana

December 2020

**THE PURDUE UNIVERSITY GRADUATE SCHOOL**  
**STATEMENT OF COMMITTEE APPROVAL**

**Dr. Vikas Tomar, Chair**

School of Aeronautics and Astronautics

**Dr. Wenbin Yu**

School of Aeronautics and Astronautics

**Dr. Tyler Tallman**

School of Aeronautics and Astronautics

**Approved by:**

Dr. Gregory A. Blaisdell

*I dedicate this dissertation to my family for instilling the importance of hard work and for supporting me in pursuing my master's degree.*

## **ACKNOWLEDGMENTS**

This project is undoubtedly an outcome of the support and guidance of many people. I would like to take this opportunity to express my thanks to those who helped me with various aspects of conducting research and the writing of this thesis. First and foremost, I would like to sincerely thank Prof. Vikas Tomar. His supervision and support enabled me to complete this research. This work would not have been possible without his support. I would also like to thank Prof. Krishna Jonnalagadda for his guidance and long technical discussions. I would also like to thank my committee members for their efforts and contributions to this work: Dr. Wenbin Yu and Dr. Tyler Tallman.

I would like to thank Abhijeet Dhiman for the long insightful discussions and his constant support in developing the experimental setup. I am greatly appreciative to support from my friends and colleagues are greatly appreciated. I thank Luis Reig, Bing Li, Leonardo Facchini, Shashank Kumar, and Risi Jaiswal for their helpful suggestions and their good-natured support. Finally, I would like to thank my parents, my brother, and my sister-in-law for their understanding, love, and moral support.

## TABLE OF CONTENTS

LIST OF TABLES .....	6
LIST OF ILLUSTRATIONS .....	7
LIST OF ABBREVIATIONS .....	9
ABSTRACT .....	10
1. INTRODUCTION .....	11
2. LITERATURE REVIEW .....	14
3. MULTI-FIDELITY MACHINE LEARNING BASED APPROACH TO PREDICT LOCAL STRAIN RESPONSE .....	18
3.1 Introduction .....	19
3.2 Nail Impact Experiment .....	19
3.2.1 Experimental Setup .....	19
3.2.2 Sample Preparation .....	21
3.2.3 Digital Image Correlation .....	23
3.2.4 Sensor Load Profile .....	27
3.3 FEM Modeling .....	31
3.3.1 Comparing Simulation with DIC Data .....	33
3.3.2 Comparing Simulation with Sensor Data .....	35
3.4 Multi-Fidelity ML model .....	37
3.4.1 Toy Model .....	39
3.4.2 Generating Dataset .....	43
3.4.3 Low-Fidelity Model .....	45
3.4.4 Multi-Fidelity Model .....	47
3.5 Conclusion .....	49
4. FUTURE WORK .....	51
REFERENCES .....	52

## LIST OF TABLES

Table 1. Material properties of PMMA .....	31
Table 2. Material properties of Brass.....	32
Table 3. Specification of HFM (Toy Model).....	39
Table 4. Specifications of LFM (Toy Model).....	41
Table 5. Specification of NN2 in the multi-fidelity model (Toy model).....	42
Table 6. Input variable to generate the low-fidelity dataset.....	43
Table 7. Specifications of LFM .....	46
Table 8. Specification for NN2 of MFM .....	48

## LIST OF ILLUSTRATIONS

Figure 1. Testing method classification based on strain rate. (reuse from [1] with permission)..	11
Figure 2 Split Hopkinson pressure bar (SHPB) experimental setup.....	12
Figure 3. Elastic v/s plastic waves in uniaxial stress (reuse from [7] with permission) .....	15
Figure 4. Boussinesq Problem .....	15
Figure 5. Impact System .....	20
Figure 6. Schematic of the complete experimental setup .....	20
Figure 7. Sample preparation method .....	22
Figure 8. Sample surface (a) Clear surface before PDMS coating (b) Surface after particle deposition before curing (c) Surface after curing .....	22
Figure 9. (a) Camera view of the sample surface (b) Gray scale distribution .....	23
Figure 10. Distribution of deformation ( $u_{xx}$ ) over the entire field of view - DIC.....	24
Figure 11. Distribution of strain ( $\epsilon_{xx}$ ) over the entire field of view - DIC.....	25
Figure 12. Variation of strain ( $\epsilon_{xx}$ ) with time and position - DIC.....	26
Figure 13. Temporal evolution of strain ( $\epsilon_{xx}$ ) at the point of local compression- DIC.....	26
Figure 14. (a) Sensor calibration setup (b) Voltage v/s Load calibration curve for sensor .....	27
Figure 15. (a) Sample reading from sensor (b) with low pass filter of 0.5MHz.....	28
Figure 16. Linearly approximating the relation between force and voltage .....	28
Figure 17. Sample load profile obtained using sensor.....	29
Figure 18. Load response under high-speed impact (Compressive force is considered as positive here) .....	29
Figure 19. Velocity profile for a weak shock wave .....	30
Figure 20. Change in the refractive index of PMMA with density .....	30
Figure 21. FEM Model of experiment .....	32
Figure 22. Convergence plot for FEM model (Strain energy (N-m) vs Number of elements).....	33
Figure 23. Elements considered to the study the variation of strain with position and time (a) Isometric view (b) Side view .....	33
Figure 24. Variation of strain ( $\epsilon_{xx}$ ) with position and time.....	34
Figure 25. Comparing simulation and DIC results .....	35

Figure 26. Elements considered for comparing results with DIC.....	35
Figure 27. (a) Elements considered to measure load response (b) Combined load profile .....	36
Figure 28. Average load profile at the back surface of the sample from simulations .....	36
Figure 29. Comparison of load response from (a) simulations with (b) sensor data (Note that the axes of the two plots are on a different scale).....	37
Figure 30. (a) Experimental v/s (b) Simulation model .....	38
Figure 31. Toy model using only high-fidelity data (a) Loss curve (b) Prediction made.....	40
Figure 32. (a) Loss curve for LFM (b) Prediction made using low-fidelity data (Toy model) ....	41
Figure 33. Neural network architecture for the multi-fidelity model (Toy Model).....	42
Figure 34. (a) Prediction made using high-fidelity alone (b) Prediction made using multi-fidelity model.....	43
Figure 35. Different simulations generated .....	44
Figure 36. Flowchart for generating the low-fidelity dataset .....	45
Figure 37. Elements considered for local response measurement while generating data.....	45
Figure 38. Activation function: ReLU v/s Leaky ReLU.....	46
Figure 39. Loss curve for the low-fidelity model .....	47
Figure 40. Sample predictions by the low-fidelity model.....	47
Figure 41. Loss curves for (a) High-fidelity model (b) Multi-fidelity model.....	48
Figure 42. Measured v/s predict strain by MFM .....	49



## **LIST OF ABBREVIATIONS**

FEM: Finite Element Method

SHPB: Split Hopkinson Pressure Bar

PMMA: Polymethyl methacrylate

ECM: Expanding cavity model

DAQ: Data acquisition

DIC: Digital Image Correlation

FSR: Force-sensitive resistor

AOI: Area of Interest

NN: Neural Network

SM: Surrogate Models

HFM: High-Fidelity Models

LFM: Low-Fidelity Models

MFMs: Multi-Fidelity Models

MSE: Mean Square Error

ReLU: Rectified Linear Unit

## ABSTRACT

High strain dynamic response of materials is of key importance for material development. An attempt was made to study the local material behavior of PMMA (polymethyl methacrylate) using a flat nail impact. The developed experiment aims to study the local material behavior by measuring the local strain and deformation response, and bulk load response. The material behavior is studied, and the prediction is made about the local material response with machine learning and predictive modeling techniques using training data set from the developed micro-scale nail impact experiment. PMMA samples were impacted with flat nails at high velocities using an in-house built gas gun. Sensors (force sensitivity resistors) are used to measure the material load response of examined samples. Digital image correlation (DIC) was used with a high-speed camera to record the local surface deformation and strains.

The aim of this work holds to understand the wave propagation in the material and to predict the material behavior of the sample under the point of impact using the sensor data. Experiments and its data processing here were expensive in terms of time and complexity and hence concurrently, a FEM simulation was developed to mimic the experiment. A large amount of FEM data was generated to create the dataset for a low-fidelity model. The experiment (and simulation) parameters and the sensor data (force profile on the back surface of the sample in case of the simulation) are used to build the training data. The model predicts the strain profile (DIC data) of the sample at the point just below the impact. Composite neural-net architecture is implemented to model to multi-fidelity approach and comparisons were made between high-fidelity and multi-fidelity prediction.

# 1. INTRODUCTION

Dynamic impact and dynamic properties hold very much importance in understanding the many phenomena, material behavior, and developing new materials. Theoretically and experimentally a lot of development has taken place, but still, there is a lot to discover and explore. Mechanical waves in solids attenuate with the distance which makes it crucial to understand the localized behavior, near the place of origin of the wave to predict the possibility of fracture or failure. This makes it important to study the localized phenomenon happening in the material.

Dynamics response is characterized and differentiated based on strain rate of impact. We have different experimental testing methods for different strain rates as the material response drastically changes and require different dynamic considerations. Figure 1 shows the common testing methods and dynamic consideration taken based on different strain rates.

STRAIN RATE $s^{-1}$	COMMON TESTING METHODS	DYNAMIC CONSIDERATION	
$10^7$	<b>HIGH VELOCITY IMPACT</b> • Explosives	SHOCK-WAVE PROPAGATION	INERTIAL FORCES IMPORTANT
$10^6$	• Normal plate impact		
	• Pulsed laser		
$10^5$	• Exploding foil	SHEAR-WAVE PROPAGATION	
	• Incl. plate impact (pressure-shear)		INERTIAL FORCES IMPORTANT
$10^4$	<b>DYNAMIC HIGH</b> • Taylor anvil tests	PLASTIC-WAVE PROPAGATION	
$10^3$	• Hopkinson Bar/ SHPB		
	• Expanding ring		
$10^2$	<b>DYNAMIC Low</b> • High-velocity hydraulic,	MECHANICAL RESONANCE IN SPECIMEN AND MACHINE IS IMPORTANT	INERTIAL FORCES NEGIGIBLE
$10^1$	• Pneumatic machines; cam		
	• Plastomer		
$10^0$	<b>QUASI-STATIC</b> • Indentation	TESTS WITH CONSTANT CROSSHEAD VELOCITY STRESS THE SAME THROUGHOUT LENGTH OF SPECIMEN	
$10^{-1}$	• Hydraulic, servo-hydraulic		INERTIAL FORCES NEGIGIBLE
$10^{-2}$	• Screw-driven testing machines		
$10^{-3}$			
$10^{-4}$			
$10^{-5}$	<b>CREEP AND STRESS RELAXATION</b> • Conventional testing machines	VISCO-PLASTIC RESPONSE OF METALS	INERTIAL FORCES NEGIGIBLE
$10^{-6}$	• Creep testers		
$10^{-7}$			

Figure 1. Testing method classification based on strain rate. (reuse from [1] with permission)

This work focuses on the dynamic response (Dynamic high in Figure 1) of materials at a strain rate of  $\sim 10^4 \text{ s}^{-1}$ . Popular methods at this strain include the Tylor anvil test, Hopkinson bar (SHPB), and expanding ring test. The Hopkinson bar experiment was developed by B. Hopkinson in 1914 [2]. Later in 1949, Kolsky modified the experiment using the Split Hopkinson Pressure Bar experiment (SHPB) or Kolsky Bar experiment [3]. Since then a lot of variants of SHPB have been developed to study a variety of materials. SHPB today is a well-known and generalized used method for the dynamic elastic-plastic response. Figure 2 shows the SHPB setup which consists of a striker bar, an incident bar, and a transmission bar, and the specimen is sandwiched between the latter two. The strain gauges provide the incident, reflected, and transmission waves which are used to calculate strain, stress, and strain rate in the material.

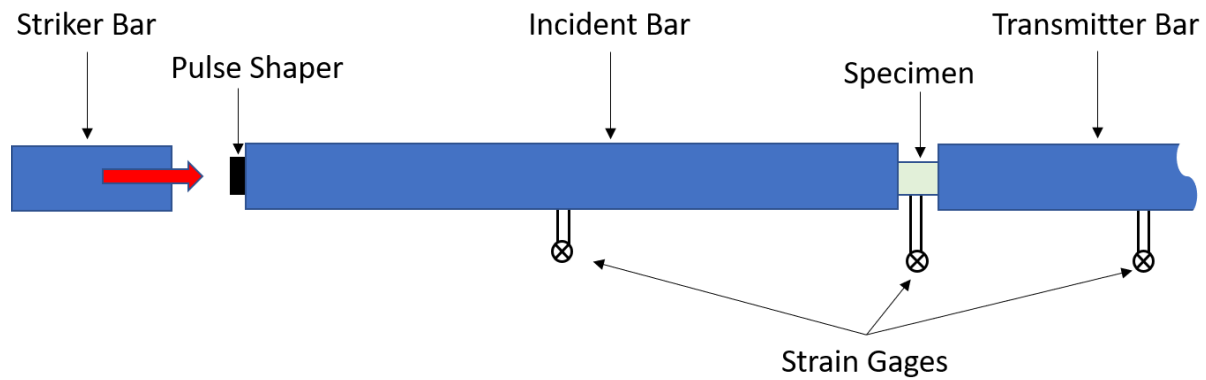


Figure 2 Split Hopkinson pressure bar (SHPB) experimental setup

The SHPB method assumes a planar condition of the bar-specimen interface. This is true for hard materials but not for soft specimens as the eigen-functions of a finite diameter bar possess high-frequency modes which are strong functions of the boundary conditions [4]. Also, the material property for the specimen is a derived quantity from strain response of incident and transmission bars. Hence, we do not measure the properties of the material *in situ*. The conventional SHPB assumes one-dimensional stress wave propagation, stress, and strain homogeneity in the deforming specimen. The latter typically does not hold for high strain rate deformation of soft and/or low impedance materials.

The common testing methods at dynamic-high strain rates, like the Tylor anvil test, Hopkinson bar (SHPB), and expanding ring test do not capture the local material information. With the intent to study local material deformation and to cater to the gaps discussed about the SHPB method, we proposed an experimental approach to predict the material properties *in situ* using a dynamic impact test in half-space. In the experiment, the impact creates local deformation, along with wave propagation in the material. The idea was to use the latter to predict the former. This was contrary to the most traditional experiments which use uniaxial loading (deformation) to study the material response. The work presented in the thesis is limited to the study and measurement of local strain and deformation to understand the material response. Constitutive modeling is not dealt with in this study.

This thesis is divided into four chapters. Chapter 1 presents an objective and holistic view of the work. Chapter 2 provides a comprehensive literature review on the dynamic impact studies done on half-space. It discusses the advantages and disadvantages of various developed analytical models. Chapter 3 presents the manuscript (under preparation) of the complete work. Chapter 3 is divided into 3 main sections. Section 3.2 describes the experimental techniques used in this work. The experimental setup and process of sample preparation developed in this work are described in detail. The key idea is to impact a flat projectile against the surface (half space) at a high velocity. DIC and sensor measurements are examined as well. Section 3.3 is a discussion of the FEM simulation developed to model the experiments and its comparison with the same. Section 3.4 is about a multi-fidelity machine learning-based approach to make predictions. A toy model of the complete approach is presented to demonstrate the working of multi-fidelity models. 1000 simulations were run to generate the low-fidelity data to predict local material behavior.

## 2. LITERATURE REVIEW

In this chapter, multiple theories have been discussed which provides different perspectives to see the problem at hand. The key objective here is to understand the local material response in half-space. Hence, we are interested to see how the material will deform dynamically under a flat impact. One approach to this problem is by understanding that how deformation occurs and how does wave propagation takes place during this impact. But also, this problem resembles with the famous Boussinesq Problem but in the dynamic domain. The expanding cavity model, though used often for quasi-static experiments can provide a certain insight into the material behavior.

Equation of Plastic waves for uniaxial stress developed by Von Karman and Duwez [5], and Taylor [6] is given by (Von Karman and Duwez used Lagrangian coordinates whereas Taylor used Eulerian coordinates but both came up with the same result)-

$$\frac{\partial u^2}{\partial t^2} = \frac{d\sigma/d\varepsilon}{\rho_o} \frac{\partial u^2}{\partial x^2}$$
$$\text{and } V_p = \left( \frac{d\sigma/d\varepsilon}{\rho_o} \right)^{\frac{1}{2}}$$

in which  $u$  is the uniaxial plastic deformation,  $\sigma$  and  $\varepsilon$  represent the stress and the strain in the material,  $\rho_o$  is the initial density of the material and  $V_p$  is the velocity of the plastic wave. We see that the velocity of the wave depends on the slope of the stress, strain curve. As the slope is maximum in the elastic region given by the young's modulus, the elastic wave has a higher velocity than plastic waves as shown in Figure 3. When the impact happens both elastic and plastic waves are produced. The former travel faster due to high velocity. As time progresses the plastic velocity decreases with decreasing work-hardening rate, there is a tendency for the front of the wave to spread out, or disperse. The attenuation also takes place as the wave moves due to loss of energy, which plays a very important role in the case of half-space is discussed in this study.

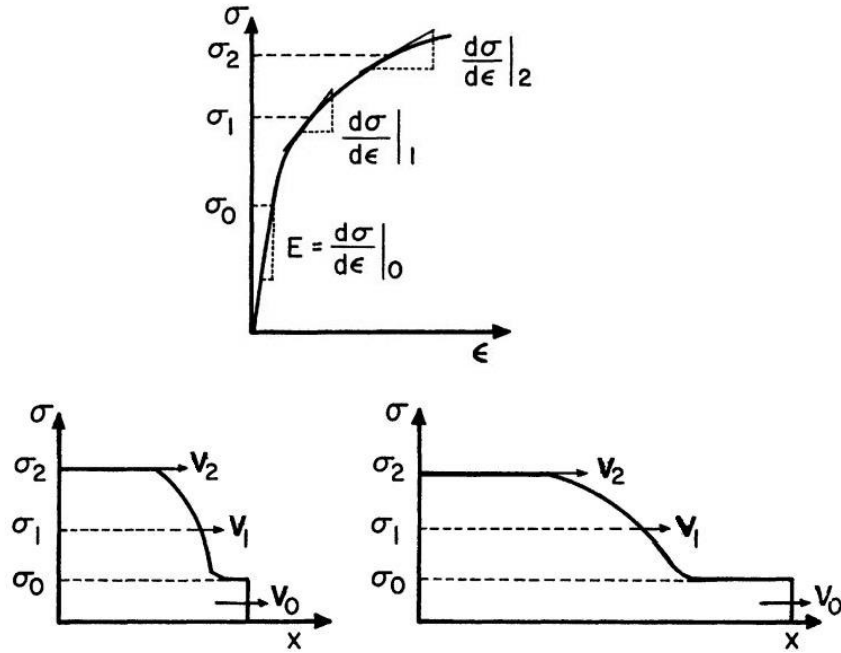


Figure 3. Elastic v/s plastic waves in uniaxial stress (reuse from [7] with permission)

Boussinesq Problem as shown in Figure 4 deals with the study of the elastic state in a linearly elastic isotropic half-space when subject to a concentrated load applied on the boundary surface and perpendicular to it [8, 9]. This is one among the most studied problem which led to the development of multiple great theories.

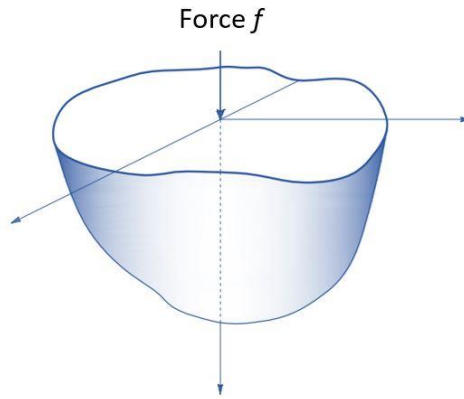


Figure 4. Boussinesq Problem

Sneddon provided a solution to the axisymmetric Boussinesq problem using the Hankel transforms and the theory of dual integral equations [10]. The boundary conditions used were-

$$\sigma_{rz}(r, 0) = 0,$$

$$u_z(r, 0) = D - f\left(\frac{r}{a}\right), \quad 0 \leq r \leq a$$

$$\sigma_{zz}(r, 0) = 0, \quad r > a$$

where  $a$  is the radius of the circle of contact, function  $f$  is referred to the tip as origin, the equation of the punch.  $D$  is the depth to which the tip penetrates in the elastic half-space.

He approximated the deformation in  $r$  (polar) and  $z$  (depth) directions using the weighted sum of an infinite number of Bessel functions of the first kind. The solution is highly simplified for the case of a flat-ended cylindrical punch and is presented here. The total load required to produce a penetration  $D$  was given by-

$$P = \frac{4\mu a D}{1 - \varphi}$$

in which  $\varphi$  is the Poisson ratio and  $\mu$  is the rigidity modulus of the material of the half-space.

The pressure distribution under the punch was given by-

$$\sigma_{zz}(r, 0) = - \frac{2\mu D}{\pi(1 - \varphi)} (a^2 - r^2)^{-\frac{1}{2}}, \quad 0 \leq r < a$$

and the shape of the deformed boundary obtained was-

$$u_z(r, 0) = \frac{2D}{\pi} \sin^{-1}\left(\frac{a}{r}\right), \quad r > a$$

One of the interesting applications of this solution was to determine the viscoelastic properties of materials by constructing the indentation load–depth relation for a cylindrical flat punch indenting into an elastic or linearly viscoelastic layer bonded to a rigid substrate [11, 12]. Analytical and simulation studies have been done to evaluate the dynamic stress in elastic half-space. These models extend the solutions to the Boussinesq problem to dynamic loads with a harmonic variation in time [13, 14].

Another point of view to understand the local response is given by the expanding cavity model (ECM). Expanding cavity models were developed by Marsh [15], Hirst and Howse [16], Johnson [17], using Hill's [18] solution for the quasi-static expansion of an internally pressurized spherical shell. These models were developed for elastic–perfectly plastic material. The model of



indentation was idealized with a hemispherical (or a semi-cylindrical) core, followed by an elastic-plastic zone. The basic idea was that the hydrostatic pressure in the core must equal the radial component of stress in the external zone at  $r = a$  and it was assumed that the volume of the material displaced by the indenter is accommodated by the radial expansion of the hemispherical core.

Various studies have been done to implement ECM models for dynamics impacts and projectile penetrations [19-21]. These models were developed on Hill's work [18]. Chadwick gave the quasi-static expansion model for spherical cavities for elastic-rigid plastic materials [22]. Hopkins [23] came up with a method for ductile metal to calculate pressure for the dynamic expansion of a cavity. His assumptions included the incompressible elastic response of target materials via Hooke's law and Tresca yield criteria for yielding. His work was built on Bishop's work [24], in which he incorporated both the material strength and the inertial resistance of the target in his work. Interestingly Chadwick and Hopkins both produced similar results, with the latter being a special case of the former. McDowell [25] and Goodier [26] developed the governing equations for dynamic cavity expansion models further developing on Hopkins and Hill's work.

### 3. MULTI-FIDELITY MACHINE LEARNING BASED APPROACH TO PREDICT LOCAL STRAIN RESPONSE

Ayush Rai<sup>1</sup>, Abhijeet Dhiman<sup>1</sup>, Krishna Jonnalagadda<sup>2</sup>, Vikas Tomar<sup>1\*</sup>

<sup>1</sup> School of Aeronautics and Astronautics, Purdue University, USA

<sup>2</sup> Mechanical Engineering, Indian Institute of Technology Bombay, INDIA

\*Corresponding author, Phone: (765)-494-3006 Fax: (765) 494-0307 Email: [tomar@purdue.edu](mailto:tomar@purdue.edu)

Manuscript Under Preparation.

#### **Abstract**

With the advancement in machine learning and predictive modeling techniques, an attempt is made to study the localized material response using a high throughput small-scale experimental data. A flat nail-impact experiment has been developed to impact flat bars on PMMA samples at high velocities. Sensors are used to measure the force at the back surface of examined samples as a function of impact velocity, nail and sample dimensions, and position of impact. Digital image correlation (DIC) is used with a high-speed camera to record surface deformation and strains. Force profiles from sensors and experiment parameters are used to develop a correlative machine learning approach to predict the local elastic strain response just below the impact. Low-fidelity simulation data was added to the high-fidelity experimental data to improve accuracy through the approach of multi-fidelity analysis. Composite deep neural network architecture is employed using a multi-fidelity model in this work that aims to model the strain profile, using the sensor profile from nail-impact experiments as input features.

**Keywords:** Dynamic Impact, Machine Learning, DIC, Multi-Fidelity

### **3.1 Introduction**

The understanding of local material response is of immense importance for the study of ballistic impacts and inhomogeneous microstructures. The current study aims to understand the wave propagation in half-space and to capture the localized material response, limited to strain and deformation history, under a flat nail impact. The objective was to predict the localized material response, given we know the force response at the back surface of the material. The development in the field of data science and machine learning in the past decade has made it possible to model complex relations to make accurate predictions. The analytical study of 1D wave propagation (elastic and plastic) is relatively simple. The complexity increases with higher dimensions and practical boundary conditions. A possible solution to model these complex relations could be that instead of developing empirical formulation from theory and then comparing it with experimental results, why not use the experimental directly to formulate the theory. A data-driven approach can provide accurate models and has been used for modeling many physical phenomena. This work leverages the potential of machine learning to predicts the localized material behavior under the impact. The time cost and complexity of the experiments make it difficult to generate a huge dataset, on the contrary, most machine learning and neural nets need a good amount of data to learn the complex functions. To tackle this problem the multi-fidelity approach was implemented. The dataset from simulations was used as low fidelity data to model the multi-fidelity deep neural net.

### **3.2 Nail Impact Experiment**

#### **3.2.1 Experimental Setup**

An in-house table-top gas gun setup was developed which uses a 100 PSI air compressor to launch the flat nails at high velocity. The impact system, as shown in Figure 5, uses a set of telescopic tubes (brass) with a decreasing radius performing the functionality of a nozzle and barrel and provides high impact velocity. Figure 6 shows the schematic of the complete experimental setup. The air compressor was connected to the impact system through a solenoid valve which is controlled by a relay switch.

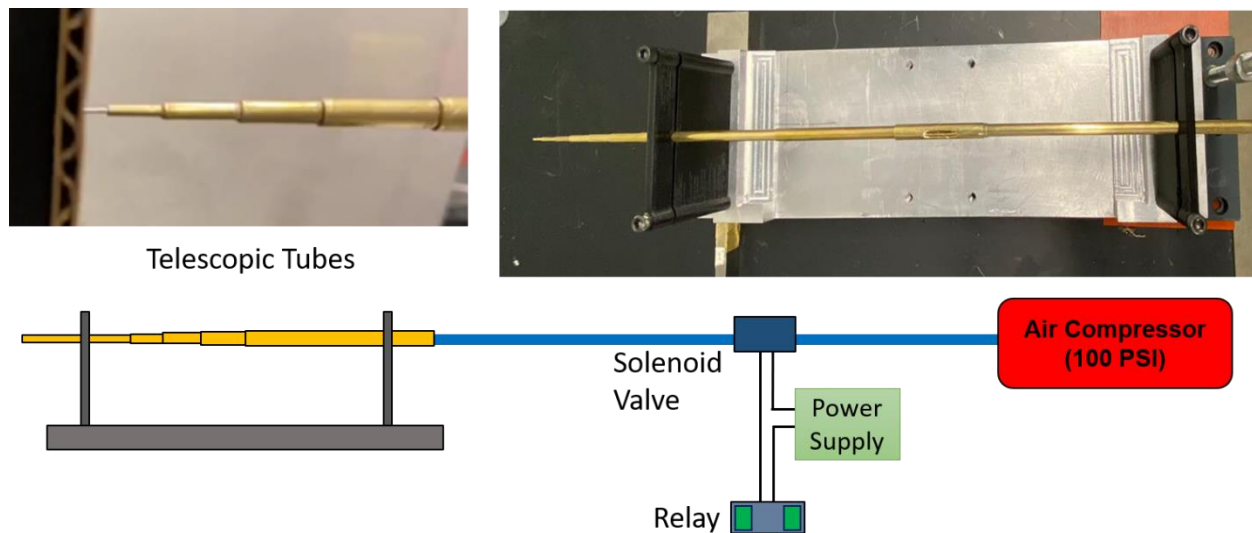


Figure 5. Impact System

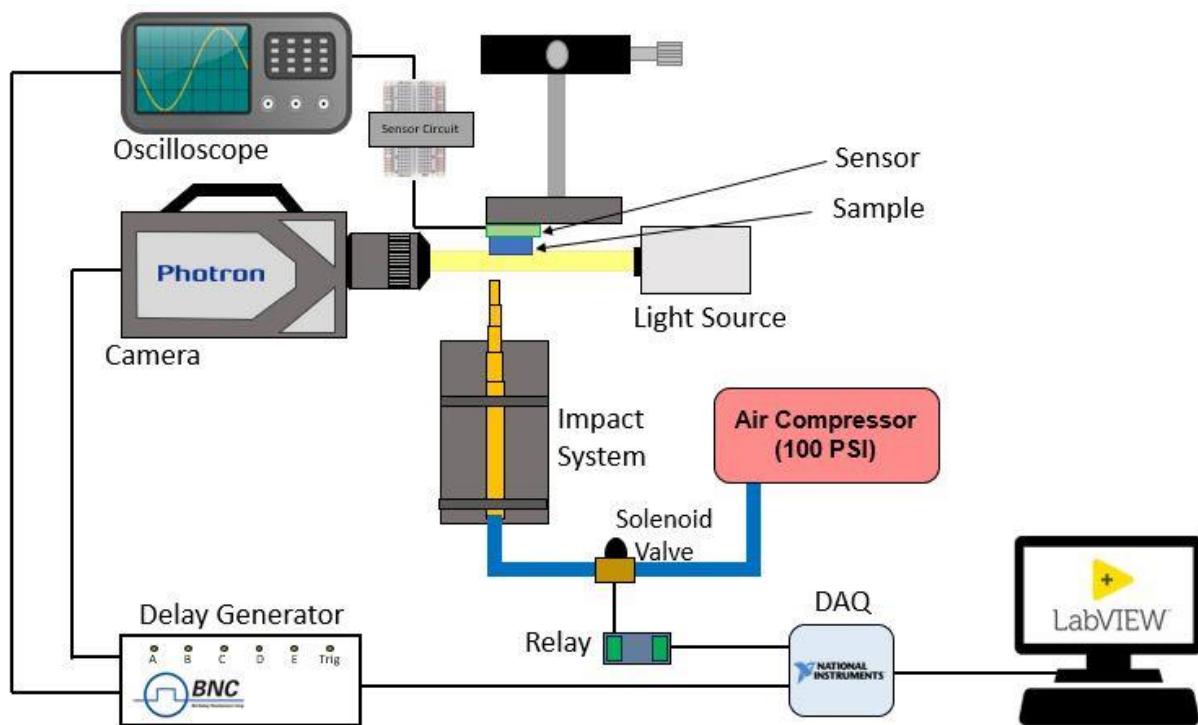


Figure 6. Schematic of the complete experimental setup

LabView was used as a central trigger to perform the experiment. Once the code on LabView is run, it triggers the DAQ (NI USB-6001 - National Instruments) which in turn triggers the relay and delay generator. The delay generator triggers the camera and the oscilloscope after a certain

delay to capture the impact data. The sample was placed on a moving stage with a fixed boundary condition on the back surface, providing it two degrees of freedom. The PMMA sample was not in direct contact with the stage instead, it was attached to the sensors which are placed on the stage using a strong adhesive. The sensors used in this experiment are force-sensitive resistors (FSRs). The experimental data includes-

- Change in strain (deformation) on the surface of the sample with time and distance: This was achieved using DIC with speckle coating on the sample. Section 3.2.3 discusses DIC calibration, experiment, and results.
- The velocity of nail impact: This velocity was calibrated based on the pressure value set on the compressor. This is because during the impact, the camera was set to capture the event at 900K frames per second and at this FPS, the resolution decreases to  $128 \times 58$  pixels with each pixel of size  $37.6 \times 37.6 \mu\text{m}^2$ . Such low resolution drastically reduces the accuracy of the velocity measurement during the impact of the camera.
- The average load response (Force) at the back surface of the sample: The sensor shows a change in resistance based on the force applied to provide a loading range from 1N to 200N with a rise time lower than 3 microseconds. Further details on sensor calibrations are discussed in section 3.2.4.

### **3.2.2 Sample Preparation**

The primary material of study here was PMMA. PMMA (Poly (methyl methacrylate)) is a colorless polymer with a glass transition temperature range of  $100^{\circ}\text{C}$  to  $130^{\circ}\text{C}$ , and a density of  $1.20 \text{ g/cm}^3$  at room temperature [27]. PMMA has good optical properties (transparent) and a high Young's Modulus. It is one of the hardest thermoplastics with high scratch resistance. It has wide applications that range from optical, pneumatic actuation, sensor, analytical separation and, biomedical applications [28-30]. PMMA has been used as one of the standard materials for the study of viscoelastic materials.

PMMA sheets of 3 mm thickness were procured from McMaster-Carr. These samples were cut and smoothened to a typical dimension of around  $8 \times 6 \text{ mm}$ . Further, PDMS was coated over the samples using a spin coater as shown in Figure 7. The samples were masked using tape before PDMS coating, all around except the top surface to keep the other surfaces intact. After coating,

Copper oxide (CuO) particles (325 mesh) was sprayed using an air spray gun by creating a particle cloud in a long vertical closed column. A repeated coating was performed by constantly checking the speckle quality under a microscope. The samples were kept at room temperature for 24 hours for PDMS to cure. Figure 8 shows the microscope images of the sample surface before PDMS coating, after speckle particle deposition, and after curing.

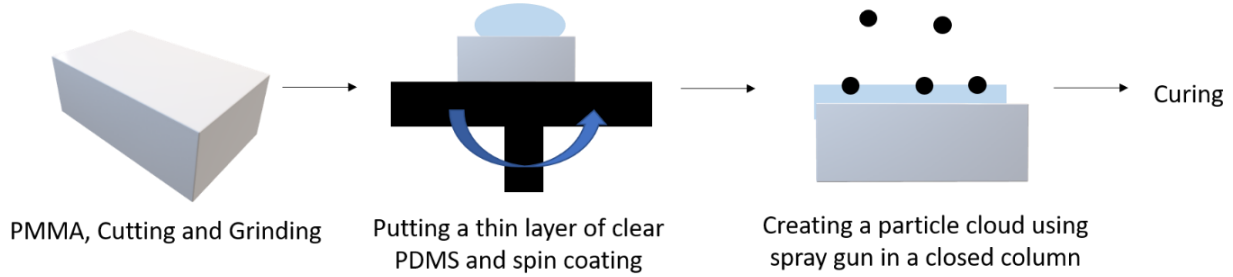


Figure 7. Sample preparation method

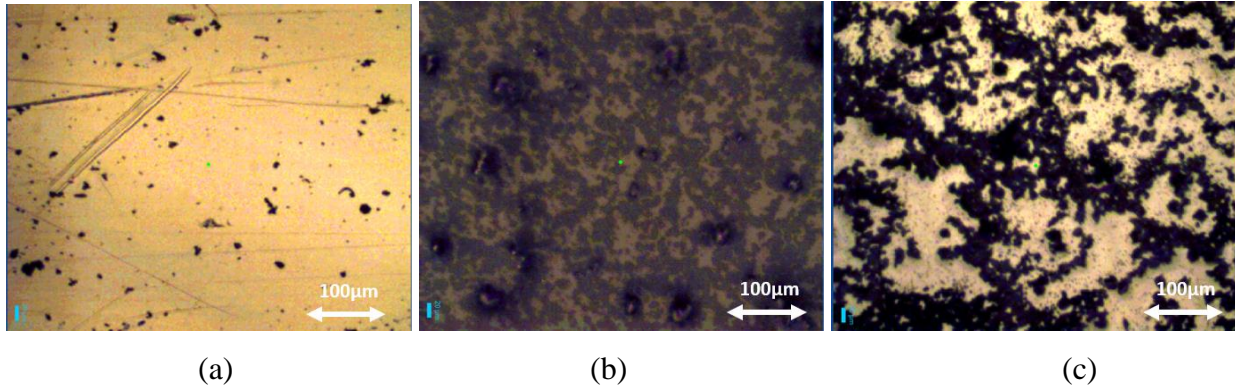


Figure 8. Sample surface (a) Clear surface before PDMS coating (b) Surface after particle deposition before curing (c) Surface after curing

Various micro-particles were experimented with for speckle patterns before deciding CuO and the mesh size. Due to the very high FPS (900K), the resolution of the images was  $128 \times 58$  pixels with each pixel size of  $37.6 \times 37.6 \mu\text{m}^2$ . Also, as the impacting nail is small relative to the sample, we do not see large deformation. The speckle was selected based on its sensitivity to capture low strains. If the particle size selected was smaller than  $30 \mu\text{m}$ , the pixel would average the intensity value making it hard to track the particles. Particle size greater than  $75 \mu\text{m}$  did not provide enough sensitivity to measure low strains in this experiment. For speckle particles, Iron oxide, Aluminum

oxide, and copper oxide were tested. The copper oxide was finally used for its better grayscale distribution.

### 3.2.3 Digital Image Correlation

Digital Image Correlation (DIC) is an optical non-contact technique used to measure the deformations and strain in material [31]. It has been used for a wide range of measurements ranging from failure studies, crack detection, wave propagation studies, and mechanobiology [32-35]. DIC is one of the popular imaging techniques for dynamic studies to measure surface deformations and strains in 2D and 3D samples.

Here DIC was implemented to measure the local strain response of the material. To capture the impact, a Photron FASTCAM SA-Z camera was used at 900K frames per second. The image resolution for frames is 128×58 pixels, with a shutter speed of 1/2880000 second. A 150W fiber optic lamphouse is used as a light source, which is placed directly across the sample as shown in Figure 6. Good speckle quality is of key importance to get good DIC data. Copper oxide particles (325 mesh) are used to obtain the speckle pattern. Figure 9 shows the sample surface on-camera frame and the corresponding grayscale distribution.

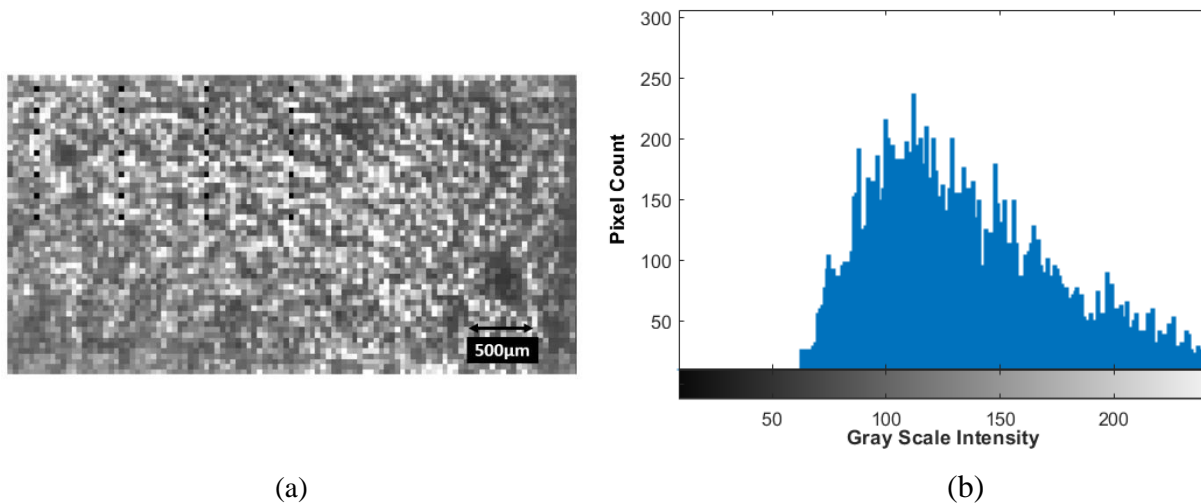


Figure 9. (a) Camera view of the sample surface (b) Gray scale distribution



Vic-2D software (Correlated Solution Inc.) was used to post-process the images after acquiring the images *in situ* to calculate deformations and strains. The subset size of  $90 \times 35$  pixels was used as AOI for DIC postprocessing. Due to the low number of pixels a subset size of 9 and a step size of 1 was used for the analysis. Gaussian weights were used for the subjects with the normalized squared difference as correlation criterion with loss pass filter. An optimized 8-tap interpolation and linear shape functions were used for the analysis. The strain field was calculated using Gaussian filtering with a filter size of 9 data points. No temporal smoothing was used for the analysis.

The results discussed here were for the nail impact experiment achieved with an impact velocity of 32m/s. The deformation and strain profiles are shown in Figure 10 and Figure 11. The maximum deformation observed here was around 30 microns. An expanding wave was observed, and the accumulation of strain took place below the nail impact. This can be explained by the fixed boundary condition at the back surface of the sample in this experimental setup.

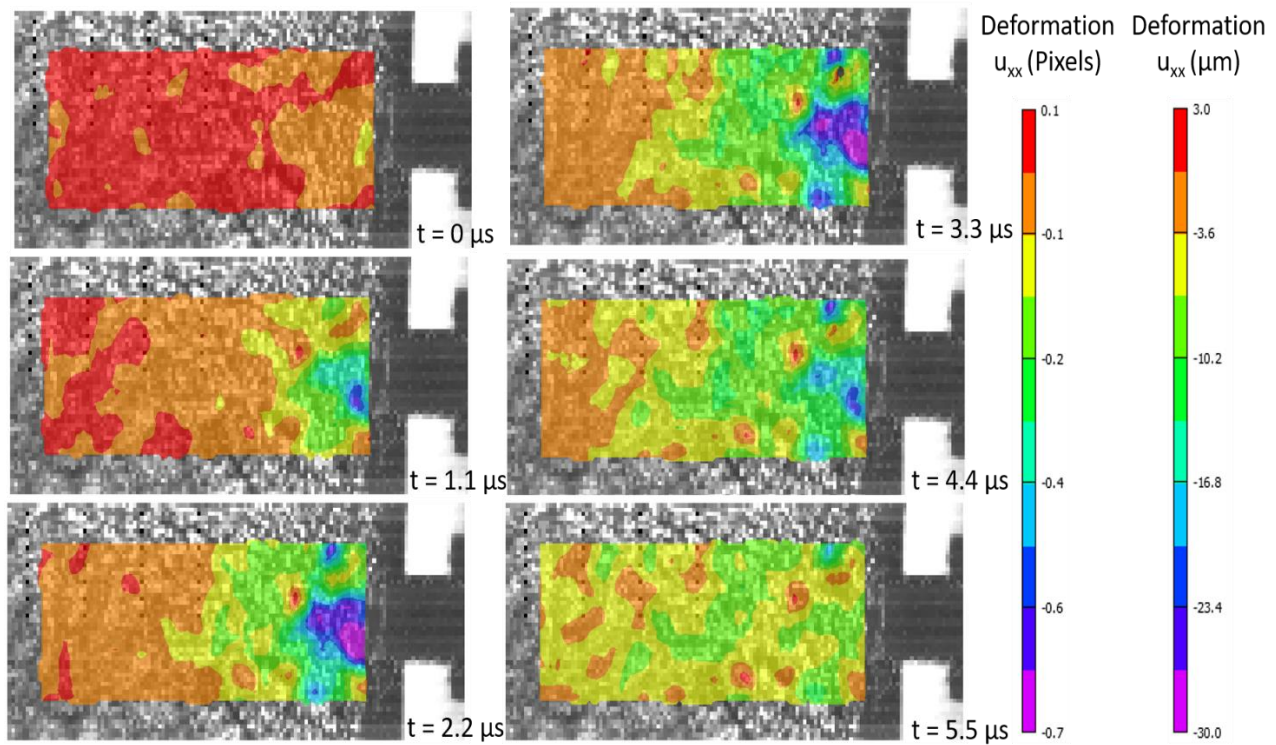


Figure 10. Distribution of deformation ( $u_{xx}$ ) over the entire field of view - DIC



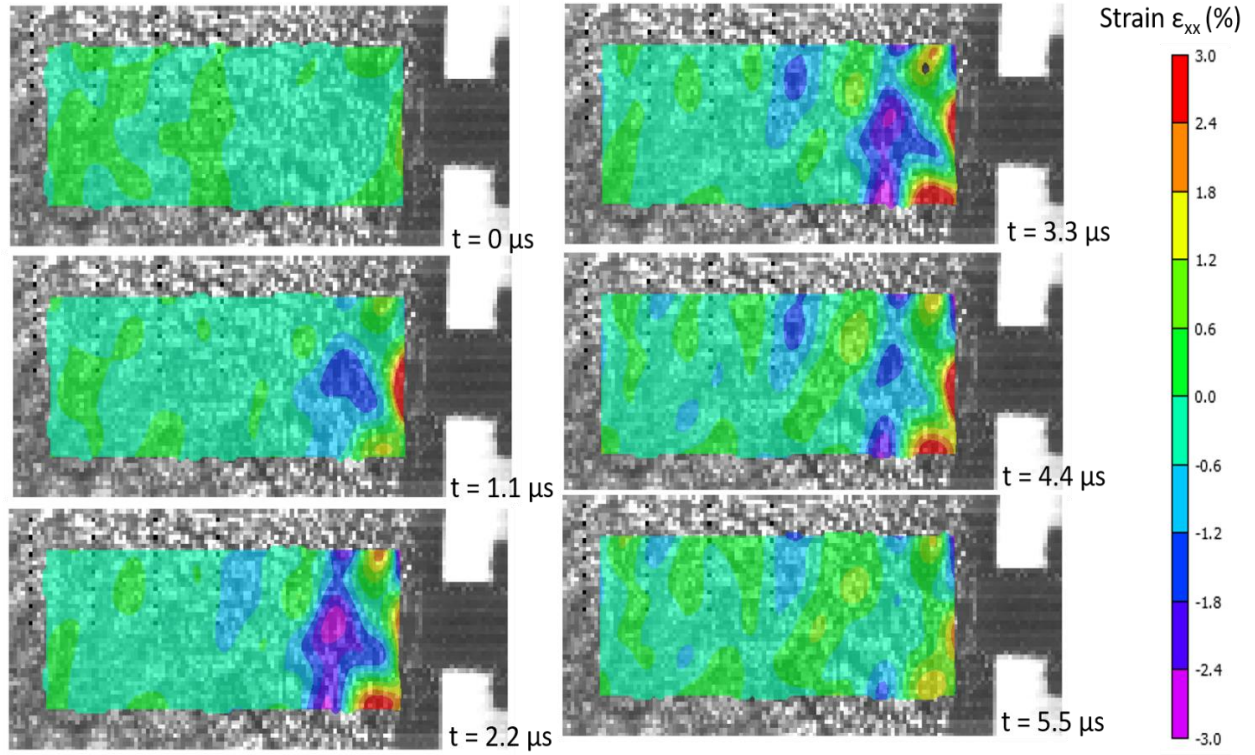
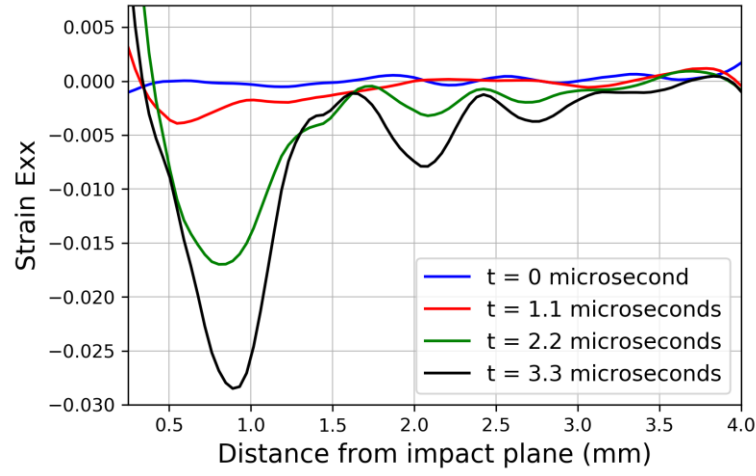
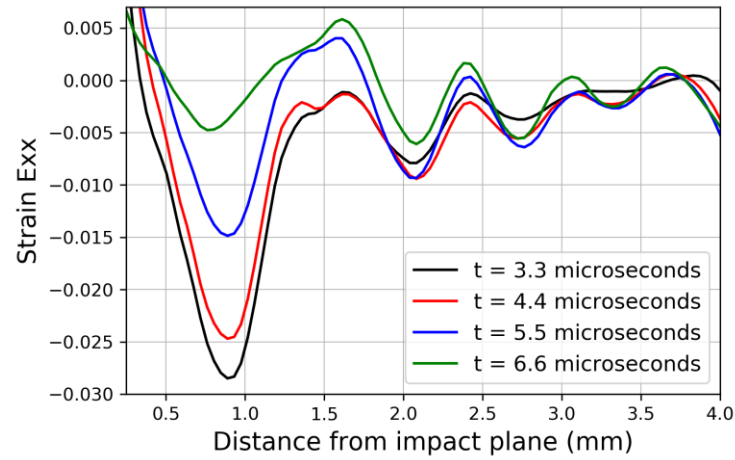


Figure 11. Distribution of strain ( $\epsilon_{xx}$ ) over the entire field of view - DIC

The plots for variation of strain with time and position are shown in Figure 12. A localized compression was observed at a distance of 0.8mm from the free surface. The maximum strain observed at this point in this experiment was  $-0.0288$ . Based on the strain v/s time plot, the temporal evolution of strain for this point (Figure 13), we see that the maximum strain rate observed here was  $1.19 \times 10^4 \text{ sec}^{-1}$  which varies with time. Further these curves are compared with FEM simulations in section 3.3.



(a)



(b)

Figure 12. Variation of strain ( $\epsilon_{xx}$ ) with time and position - DIC

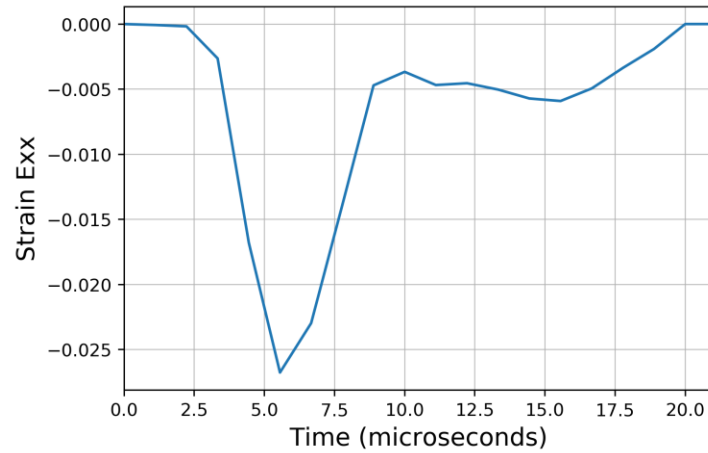


Figure 13. Temporal evolution of strain ( $\epsilon_{xx}$ ) at the point of local compression- DIC

### 3.2.4 Sensor Load Profile

The sensors used in this experiment were force-sensitive resistors (FSR UX 400), obtained from Interlink Electronics. The sensor comprises of a conductive layer, spacer, and FSR layer. When force is applied, the distance between the conductive layer and the FSR layer decreases compressing the spacer which leads to a change in resistance across the sensor. The sensor works as a variable resistor whose resistance varies from  $1\text{M}\Omega$  to  $\sim 5000\Omega$  as a function of the force applied. To use the sensor, a  $10\text{K}\Omega$  resistor was placed in parallel, with the sensor behaving as a potential divider. The voltage was measured across a  $10\text{K}\Omega$  resistor using a Tektronix oscilloscope with a high impedance buffer amplifier. The sensor was calibrated using a mechanical loading stage from Deben UK Ltd. For calibration, the load was applied using a flat punch, varying from 0-200N as shown in Figure 14.

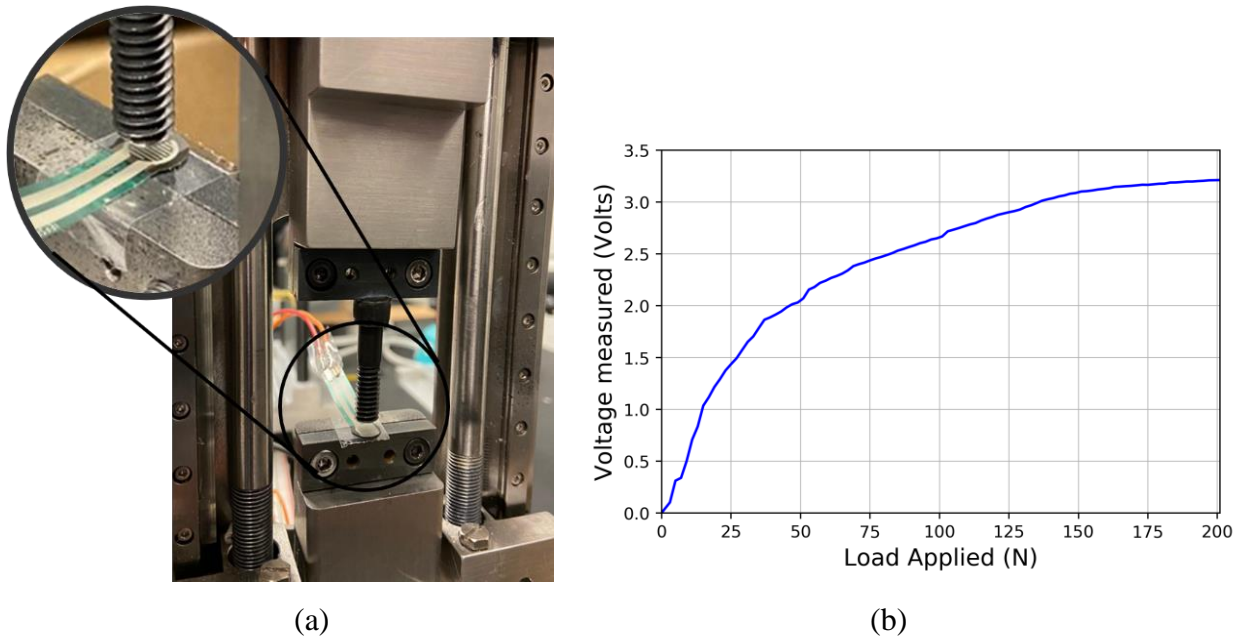


Figure 14. (a) Sensor calibration setup (b) Voltage v/s Load calibration curve for sensor

The sensor was attached to the sample and the moving stage using a strong adhesive. A typical voltage reading observed on the oscilloscope is shown in Figure 15(a). The signal was further processed using a signal processing library to cut off the noise of 0.5MHz and above. The filtered signal is shown in Figure 15(b). Here we had to obtain the force observed at the back surface of the sample from the voltage reading. For this, the calibration curve (Figure 14 (b)) was inverted.

For all our experiments, the region of interest was from 0 to 1V. As shown in Figure 16, the relation between the voltage and load for our region of interest can be approximated linearly. Hence a factor of 16.5 was used to perform the transformation between the two parameters. The response is also inverted to show the compressive nature of the force. After transforming the typical curve shown in Figure 15(b), the load response obtained is presented in Figure 17. We observe that the loading trough lasts for 30 milliseconds.

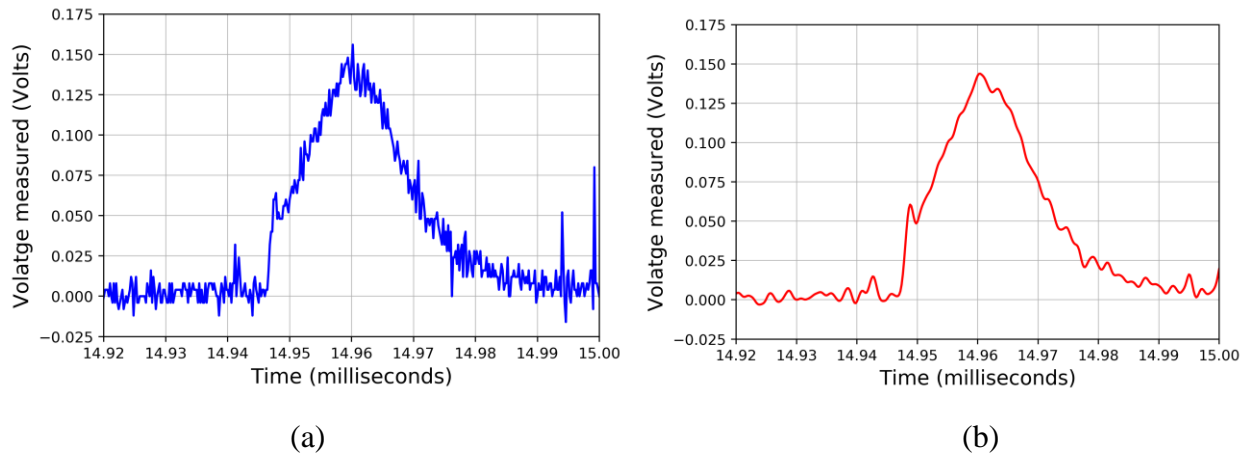


Figure 15. (a) Sample reading from sensor (b) with low pass filter of 0.5MHz

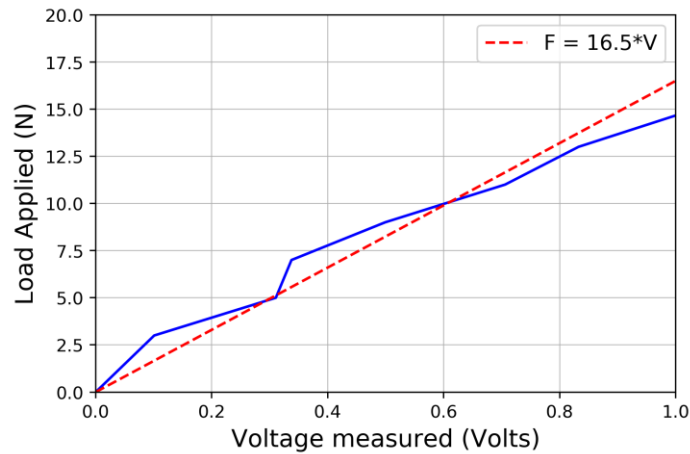


Figure 16. Linearly approximating the relation between force and voltage

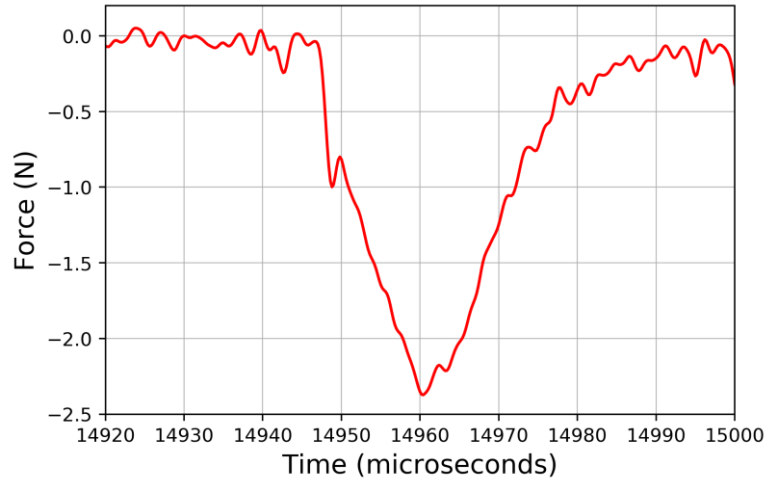


Figure 17. Sample load profile obtained using sensor

At high velocities, an interesting phenomenon was observed. As shown in Figure 18, we see two peaks in the load profile. A minute trough can also be observed in Figure 17. This is because of the elastic-plastic behavior of PMMA around the point of impact.

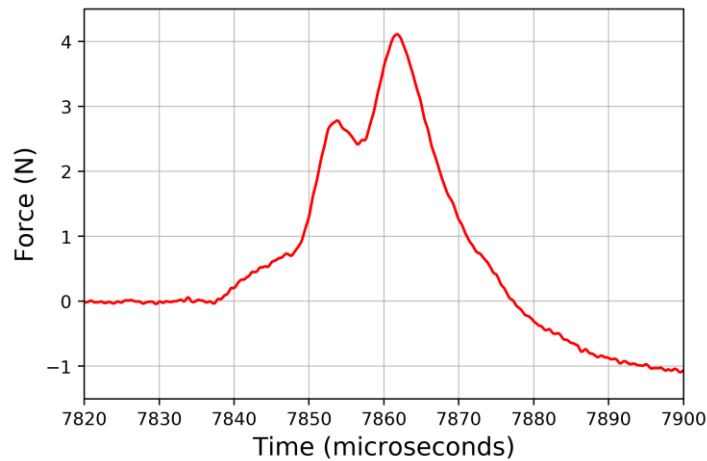


Figure 18. Load response under high-speed impact (Compressive force is considered as positive here)

To understand these peaks, we will use the concept of a weak shock wave. Grady [36] showed the realistic weak shock wave response looks like Figure 19. Initially, there is a steep rise in pressure after the Hugoniot Elastic Limit (HEL) is reached. After which there is a continuous rise in pressure which is governed by the constitutive behavior of the material. Following which there a

phase transition zone (if applicable) followed by a stable shock wave. The unloading starts elastically followed by plastically. The velocity (stress is a quadratic function of velocity but has a similar profile) for a weak shock wave is shown in Figure 19 (adapted from Grady [36]).

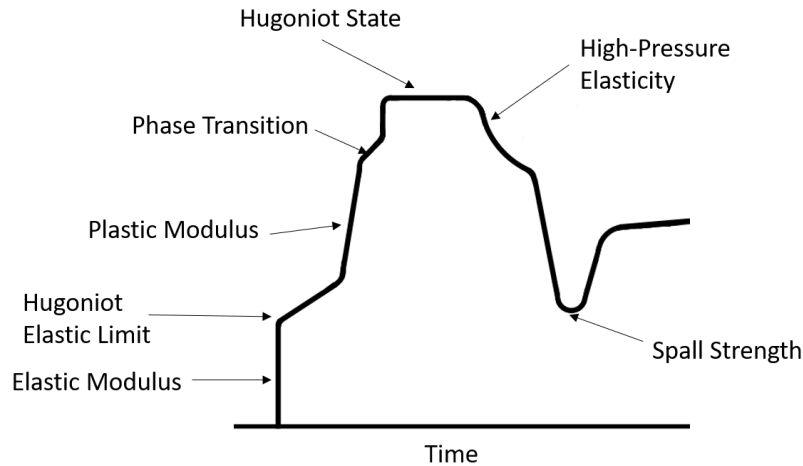


Figure 19. Velocity profile for a weak shock wave

Now in our case, a plastic wave is generated but it decays down very quickly. This can be observed on a clear sample after the impact, as the plastic wave changes the density which in turn changes the refractive index of PMMA. This property of the material is known as birefringence. Birefringence on PMMA has been extensively studied by past researchers but mostly for uniform compression case [37-40]. Figure 20 shows the change in the refractive index with plastic strain in this experiment. The depth of the plastic wave observed was  $\sim 0.1\text{mm}$



Figure 20. Change in the refractive index of PMMA with density

The first peak observed in Figure 18 shows the pure elastic wave reaching the sample. On the contrary, the second peak denotes a wave that started as a weak shock wave (plastic) but attenuated during the propagation in the sample. This also justifies the increased intensity of the second wave as compared to another. This difference becomes less at lower velocities where the two get merged and we observe a single wave. Further work is required to explore this behavior in detail. Another possible explanation that can be given [41] is that during this time, the impact force is mostly consumed in accelerating the specimen, rather than deforming it. The total impact force drops due to the reversion of the stress wave in the specimen. The impact force reaches a local minimum and then continues to build up again upon the second reverberation of the stress wave. This possibility was ruled out based on the load response observed on Quartz, where one single peak was observed at all velocities. Quartz is a highly brittle material with very high strength. Quartz typically fractures before undergoing any plastic deformation and no such failure was observed in the experiment.

### 3.3 FEM Modeling

A finite element simulation was carried out to model the impact experiment. This was developed in ABAQUS Explicit and calibrated by comparing the experimental values. The sample of dimension  $8.0 \times 6.0 \times 3.0$  mm with material properties of PMMS and a flat cylindrical nail of 0.8mm diameter and 2.0 mm length with material properties of brass was used in this simulation, which was the same as used in the experiments. The material properties of PMMA and Brass are provided in Table 1 and Table 2. The flat nail with a predefined velocity of 32m/s was impacted at the center of the sample, with 0.1mm distance from the edge as shown in Figure 21. The back surface of the samples was constrained to zero deformation in the x-direction.

Table 1. Material properties of PMMA

Young's Modulus	2855 MPa
Poisson's Ratio	0.36
Density	1190.24 kg/m <sup>3</sup>
Compressive Yield Strength	102 MPa

Table 2. Material properties of Brass

Young's Modulus	110.316 GPa
Poisson's Ratio	0.318
Density	8525.41 kg/m <sup>3</sup>

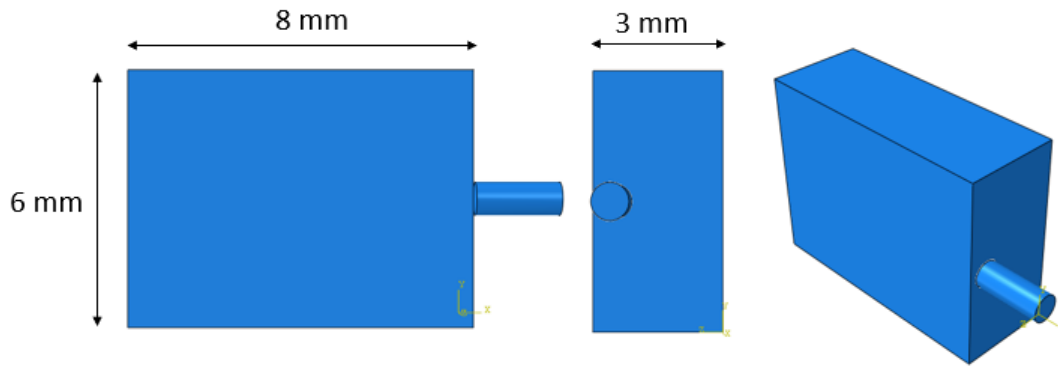


Figure 21. FEM Model of experiment

PMMA samples are modeled using C3D8R elements (8-node linear brick with reduced integration and hourglass control). The convergence of the model was checked using the maximum strain energy with an increasing number of elements. Figure 22 shows the convergence plot where the change in strain energy was not significant above 20 thousand elements. Therefore, around 20 thousand elements were used for this study. This strain profile was what we will be predicting and was the main value of interest for us and hence strain energy was used as the convergence parameter.



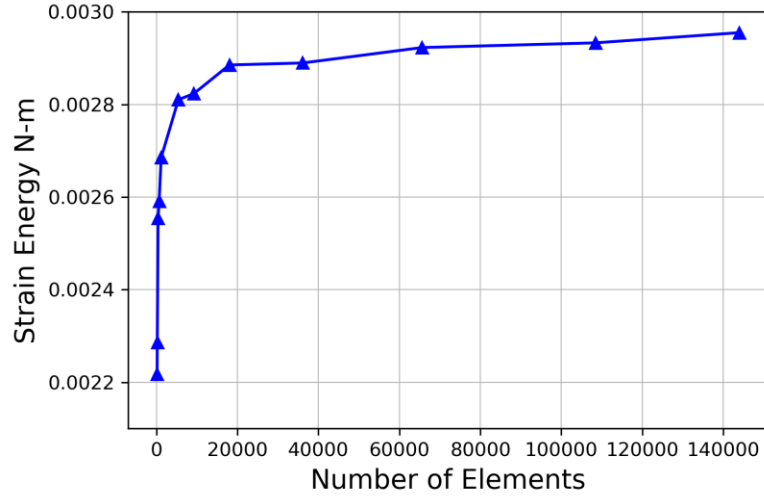


Figure 22. Convergence plot for FEM model (Strain energy (N-m) vs Number of elements)

### 3.3.1 Comparing Simulation with DIC Data

The variation of strain with position along the depth was studied at various timings across the simulation. Elements on the surface along the axis of impact were used for this study as shown in Figure 23 for studying the surface deformation, similar to the DIC measurements done in section 3.2.3. Figure 24 shows the strain ( $\epsilon_{xx}$ ) in different positions and at different time steps. We see that localized compression took place at a distance of 0.5 mm from the impact plane. A similar observation was made in DIC results (refer to Figure 11). These elements (0.5 mm from the impact plane along the axis) will be used further to compare with DIC results. The strain ( $\epsilon_{xx}$ ) increases at compression point till 6 micro-seconds and after which the material relaxes.

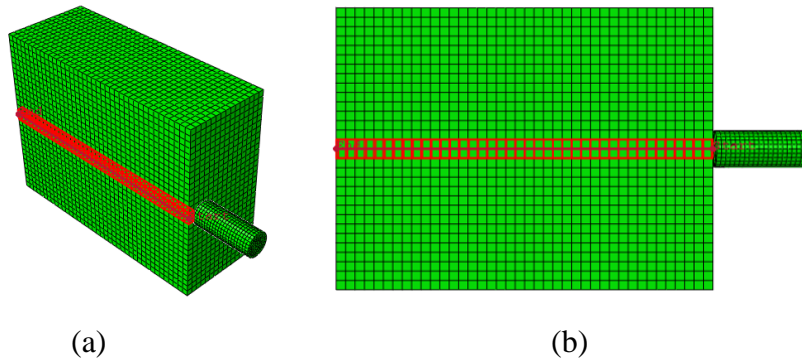
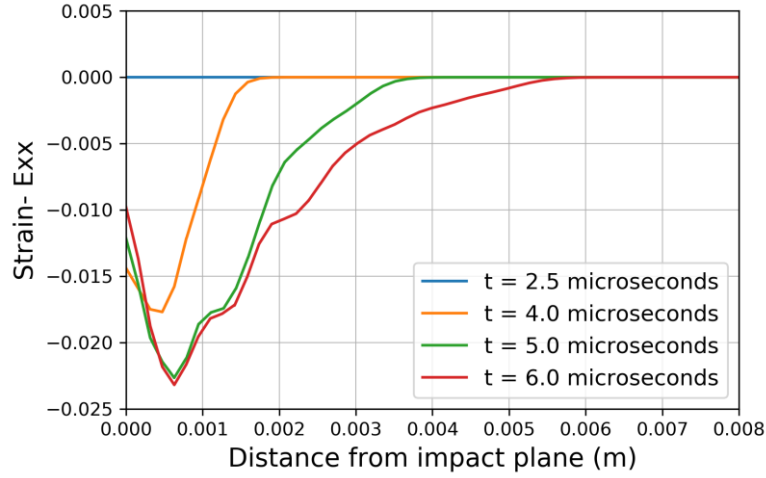
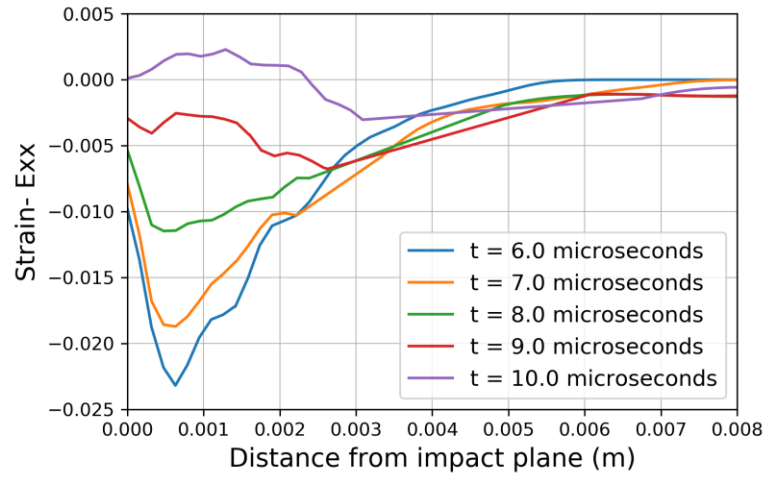


Figure 23. Elements considered to study the variation of strain with position and time (a) Isometric view (b) Side view



(a)



(b)

Figure 24. Variation of strain ( $\epsilon_{xx}$ ) with position and time

The DIC data and the simulation results are compared in Figure 25. For this comparison in simulation, the average strain of 6 elements was taken as shown in Figure 26. The simulation and DIC results match well. We see that the simulation underpredicts the maximum compressive strain, but the difference is reasonable because of model simplification.

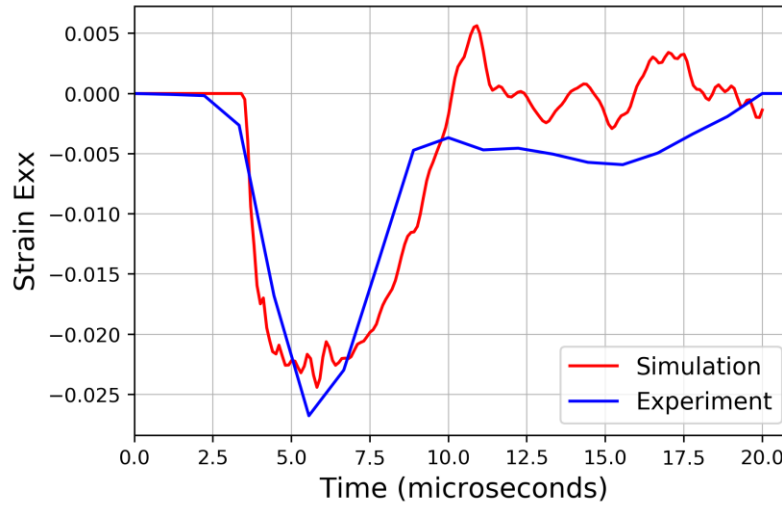


Figure 25. Comparing simulation and DIC results

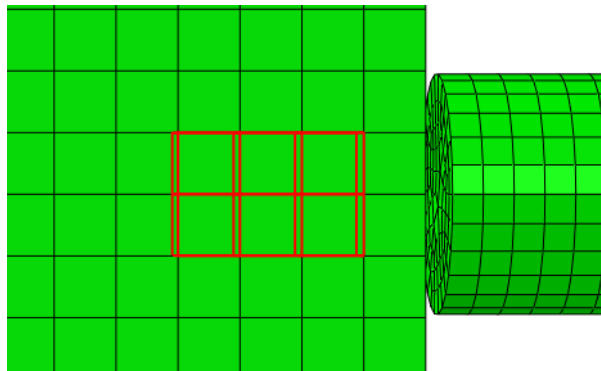


Figure 26. Elements considered for comparing results with DIC

### 3.3.2 Comparing Simulation with Sensor Data

For comparing the load profile measured by the sensor, the average force on the elements was at the back surface of the sample was calculated. Figure 27 shows the elements considered and for the comparison and the combined stress profile of all the elements. Figure 28 shows the average load response for the sample. Force profiles of elements considered vary a lot, and the uniform average was expected to just provide an approximate profile.

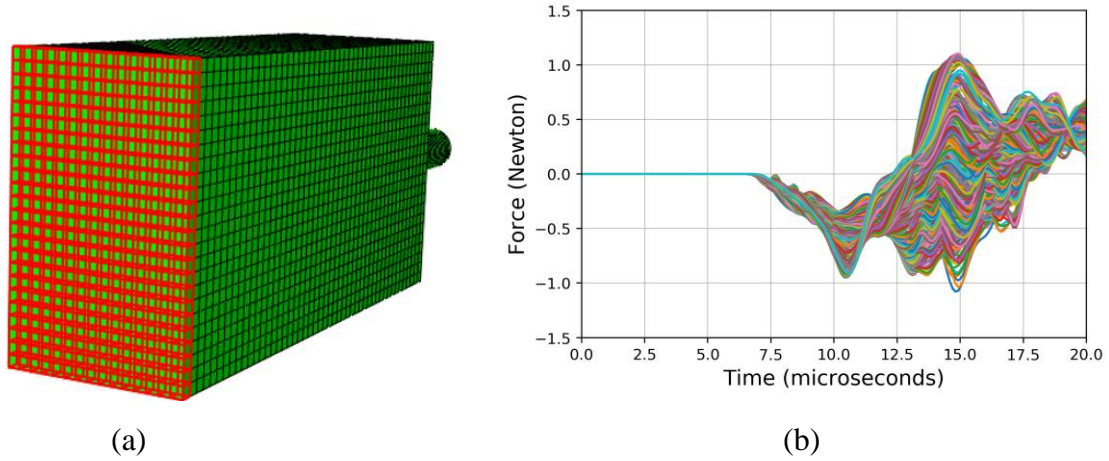


Figure 27. (a) Elements considered to measure load response (b) Combined load profile

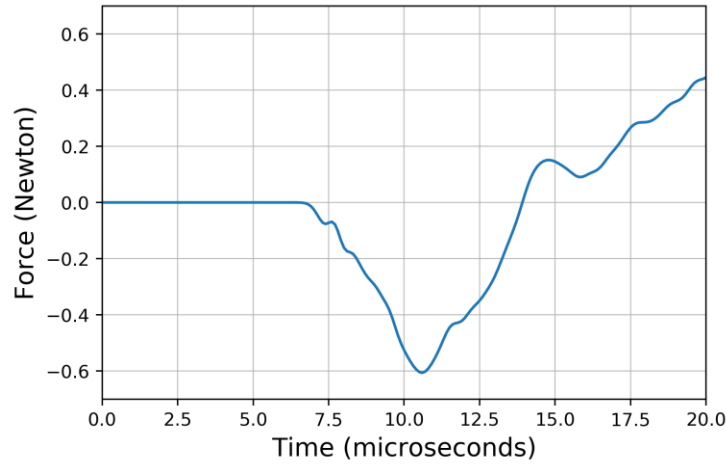


Figure 28. Average load profile at the back surface of the sample from simulations

The sensor reading and simulation data are compared in Figure 29. Note that the axes of the two plots are on a different scale. We observe the following-

- The duration of the load profile for simulation is 10 micro-seconds as compared to the sensor profile which is 30 microseconds. The rising time of the sensor presented in the datasheet is less than 3 micro-seconds. The time-sensitivity of the sensor lead to a lag in load measurement and most likely it relaxed the stress wave.
- The simulation highly underpredicts the force value (-0.76 N as compared to -4.2 N). One of the possible reasons is because of the force created by the air pressure at the back of the impacted nail in the experiment. To maximize the impact strength and to ensure a flat

impact of the nail, the sample is placed close enough to the impact system, so that nail does not do the free projectile motion. Hence it is not just the velocity but also the air pressure which creates this impact. Modeling the airflow is complex and is considered for future work.

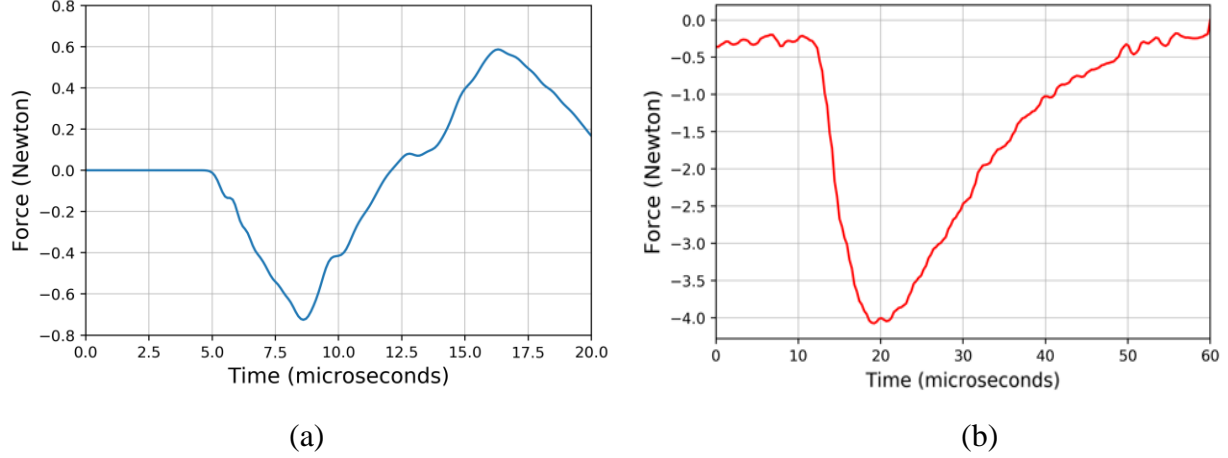


Figure 29. Comparison of load response from (a) simulations with (b) sensor data (Note that the axes of the two plots are on a different scale)

These discrepancies in the data were expected as our simulation models the sample material response and not of sample-sensor pair. As discussed in section 3.2.4, the compression of the spacer creates a change in resistance in the sensor corresponding to the force applied. Hence, the boundary condition of the sample was not completely rigid. On the contrary, the simulation assumes a perfectly rigid boundary. Despite this, these simulations give a good correlation between the load profile at the back of the sample and local strain response below the nail impact, which was used to create a low fidelity model of the experiment. Modeling sensor into the simulation will increase the accuracy of the simulated data and was considered as future work.

### 3.4 Multi-Fidelity ML model

A data-driven approach was used here to model the impact experiment. Given the sensor data, the prediction was made on the material response under the nail impact. The material response included how local stress and strain change with time during the impact, and not its material

properties. The work tried to study the decay in stress wave as a function of length and dimensions of the sample, nail velocity, and point of impact.

Fidelity refers to the reliability of the data. It is the degree to which a model or simulation reproduces real-world behavior. High-fidelity models are the behavior of the system with a high level of accuracy (concerning the application intended). These models are usually expensive in terms of cost, time, and complexity. Low-fidelity models on the contrary are an approximation to real-world relation or function. These models cheaper and less accurate hence can be generated in abundance. In this work, the experiments are the high-fidelity models (HFMs) and are assumed to show the true material response. The FEM simulations performed are a simplified approximation of the experiments providing the low-fidelity relation. (Figure 30)



Figure 30. (a) Experimental v/s (b) Simulation model

Multi-fidelity modeling provides efficient and effective use of low fidelity data by leveraging the relationship between the low- and high-fidelity data. We exploit the relationships between different fidelities to combinedly estimate the objective function of the true relation to improving the performance. The high-fidelity data are the few experimental measurements, which are hard to obtain. These are combined with synthetic data obtained from the computational model. These computation models are called surrogate models (SM). Multi-fidelity modeling can also be done without surrogate modeling by using an adaptive sampling approach [42]. The hypothesis here is that the low-fidelity data supplies high approximation trends for high-fidelity data. Various models have developed in the literature to explore the concept of multi-fidelity modeling. A few such implementations include-

- Response surface models [43, 44]
- Polynomial chaos expansion [45, 46]
- Gaussian process regression (GPR) [47-50]
- Artificial neural networks [51]
- Moving least squares

Here the multi-fidelity approach was applied using artificial neural networks. The neural networks were stacked one after another with each NN models corresponding to one fidelity. Now each fidelity was fed with both the original input and output from the previous fidelity. Each NN was trained with its fidelity data and output results of previous NNs.

### 3.4.1 Toy Model

To understand the working of the multi-fidelity model, a toy model is demonstrated here. We wish to model the one dimensional,  $\sin(x)$  function using the approach of multi-fidelity models. First, we directly try to model the function (HFM). For this, we generated 20 random values of  $x \in [0,6]$ , which are the inputs to our HFM. The function we want to predict here is  $\sin(x)$ . A NN was developed using 3 hidden layers each with 10 neurons each. Mean square error was taken as loss criteria with no other regularization term. All the specifications used for training the NN are provided in Table 3.

Table 3. Specification of HFM (Toy Model)

#Input (Features)	1 (x)
#Output (Target)	1 ( $\sin(x)$ )
Number of Samples	20
Hidden Layers	[10, 10, 10]
Learning Rate	0.001
Optimizer	Adam
Error Loss	MSE (Mean square error)
Epochs run	100

Figure 31(a) shows the training loss curve of the learned NN. The MSE decreases with epochs, stabilizing at around 65 iterations. Figure 31(b) shows the prediction made by the neural network with high fidelity data. The NN was able to understand a very generic trend but providing very poor performance.

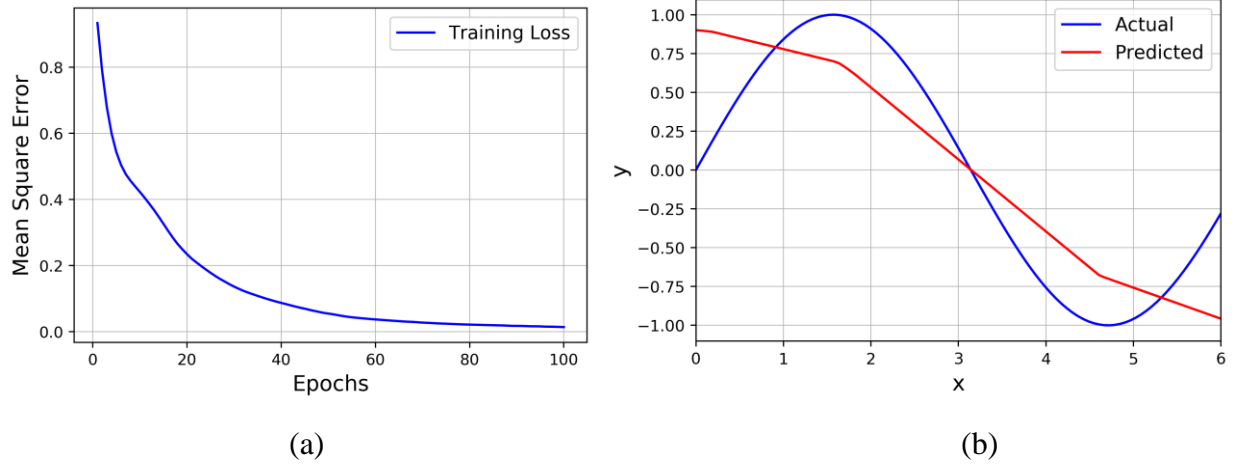


Figure 31. Toy model using only high-fidelity data (a) Loss curve (b) Prediction made

Now using the same high-fidelity data, we tried to improve the accuracy of the prediction by using the low-fidelity model. We know that the Tylor series expansion of  $\sin(x)$  is given as-

$$\begin{aligned}\sin(x) &= \sum_{n=1}^{\infty} (-1)^{(n-1)} \frac{x^{2n-1}}{(2n-1)!} \\ &= x - \frac{x^3}{3!} + \frac{x^5}{5!} - \frac{x^7}{7!} + \frac{x^9}{9!} - \dots\end{aligned}$$

To generate low-fidelity data we try to approximate  $\sin(x)$  using the first 4 terms of its Tylor expansion-

$$F(x) = x - \frac{x^3}{3!} + \frac{x^5}{5!} - \frac{x^7}{7!}$$

We generated 100 random values of  $x \in [0,6]$ , and calculated 100 corresponding target values using  $F(x)$ . Low fidelity data is cheap and hence usually present in abundance. A NN was developed using the specifications mentioned in Table 4. Figure 32 shows the prediction made by low fidelity data. The prediction is not compared with  $\sin(x)$  as the values way off and much beyond -1.  $F(x)$



over here just works as an intermediary approximation and its original value is not of much importance to us.

Table 4. Specifications of LFM (Toy Model)

Input (Features)	1 (x)
Output (Target)	1 (F(x))
Number of Samples	100
Hidden Layers	[10, 10, 10]
Learning Rate	0.001
Optimizer	Adam
Error Loss	MSE (Mean square error)
Epochs run	100

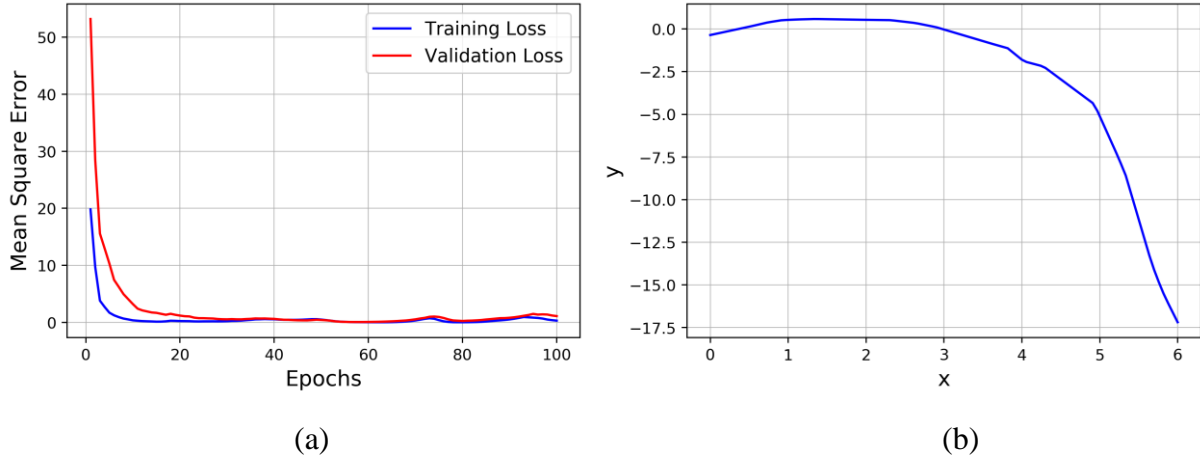


Figure 32. (a) Loss curve for LFM (b) Prediction made using low-fidelity data (Toy model)

The multi-fidelity model takes leverage of the low-fidelity data by trying to co-relate the high and low-fidelity models. The multi-fidelity model was implemented using the NN architecture presented in Figure 33. The NN1 represents the low-fidelity NN (already trained using the low-fidelity data) with specifications mentioned in Table 4. The NN2 takes two inputs, one as original input from-high fidelity data and the other as the output of NN1. The specification of NN2 is presented in Table 5. Note that here we are using high-fidelity data. The NN2 architecture is further simplified to 2 hidden layers with 10 neurons each.

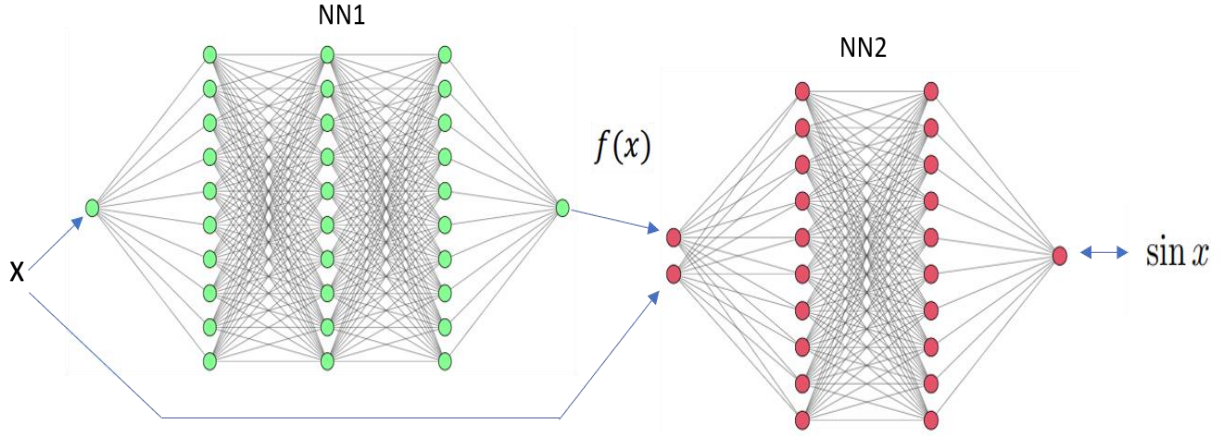


Figure 33. Neural network architecture for the multi-fidelity model (Toy Model)

Table 5. Specification of NN2 in the multi-fidelity model (Toy model)

#Input (Features)	2 ( $[\hat{F}(x), x]$ )
#Output (Target)	1 ( $\sin(x)$ )
Number of Samples	20
Hidden Layers	[10, 10]
Learning Rate	0.001
Optimizer	Adam
Error Loss	MSE (Mean square error)
Epochs run	50

The resulting prediction of the multi-fidelity model is shown in Figure 34. We observe drastic improvements in the accuracy of the prediction made. The prediction based on high-fidelity data alone only provides a generic, highly simplified trend of the actual function. On the contrary, the multi-fidelity model was able to reasonably approximate a highly non-linear function with as low as 20 points. Note that number of hidden layers, and the number of neurons used for each layer has a strong effect on the performance of the neural networks [52, 53]. In this toy model, the neurons in hidden layers are kept constants for a proper comparison and understanding. The toy model shows the potential of a multi-fidelity model to predict complex function using few high-fidelity data.

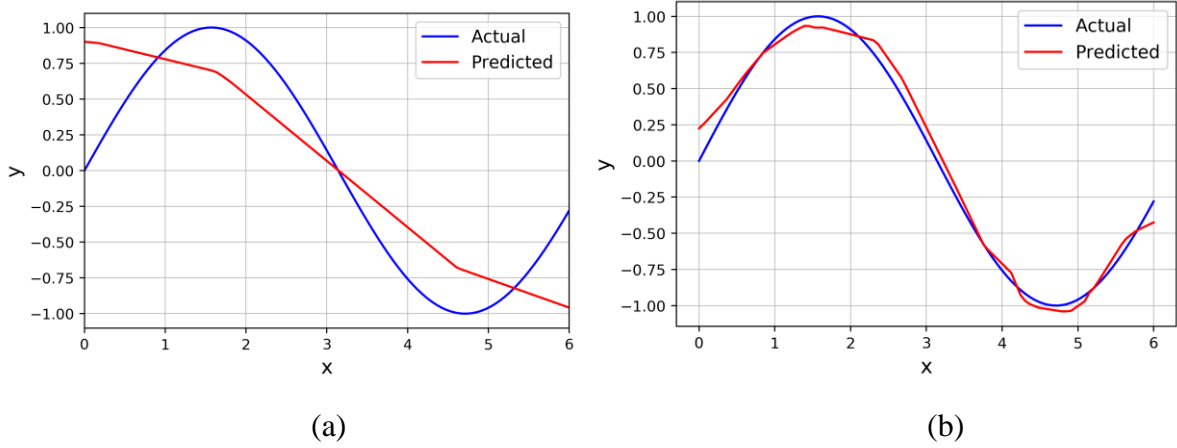


Figure 34. (a) Prediction made using high-fidelity alone (b) Prediction made using multi-fidelity model

### 3.4.2 Generating Dataset

For experimental data, 30 experiments were performed with different samples, different nails, and nail velocity from 20-45 m/s. The position of impact was also varied to obtain versatile data. The data was processed similarly as explained in session 3.2.3 and 3.2.4. The sensor data was uniformly sampled to 201 points, and the DIC data was taken directly for 21 timesteps during the impact. As each experiment requires its processing and because of the uncertainty of the time of impact with respect to the time the solenoid was triggered, the data is expensive in terms of time and complexity.

Table 6. Input variable to generate the low-fidelity dataset

Input Parameters	Range
Depth of Sample	6 – 10 mm
Length of Sample	3 – 7 mm
Length of Nail	1 – 2 mm (4.1 – 8.2 $\mu$ g)
Velocity of Nail	20 – 60 m/s
Point of Impact	Between the center and the bottom edge

The low-fidelity data was acquired by performing FEM simulations. The same boundary conditions were used for these models as discussed in section 3.3. To create the dataset, 5

parameters were changed at random which include the length of the sample, depth of the sample, length of the nail, velocity of the nail, and point of impact. The range used for these variables is provided in Table 6. Figure 35 shows a few models developed at random.

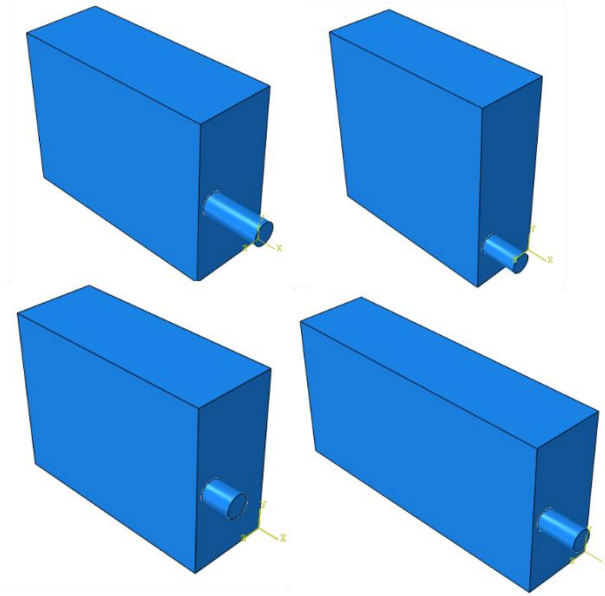


Figure 35. Different simulations generated

The data set was generated using Abaqus scripting. Scripting is a powerful tool provide by Abaqus to generate the input files and to run the simulations [ABAQUS 6.14 Scripting user's guide]. A python script was generated with all the variable parameters mentioned above to produce 1000 input files. The input files were run on the cluster and two other scripts were used to post-process the output odb files and to generate the features and target values for the ML model respectively. The complete flowchart of the data generation is presented in Figure 36.

Getting the local strain values from the simulation was a little challenging as the complete models get generated at random. For this, all the FEM model was implemented with constant mesh size in such a way, that the nail center always lies in front of the middle of the sample element. The meshing order was calculated using the sample dimensions and point of impact information was used to obtain the exact elements which need to be considered to calculate the local strain response. An example of the process is shown in Figure 37. The same method was used to obtain the average

local strain and load response as described in section 3.3. Both the response profiles were uniformly sampled to get a vector of dimension [201] each.

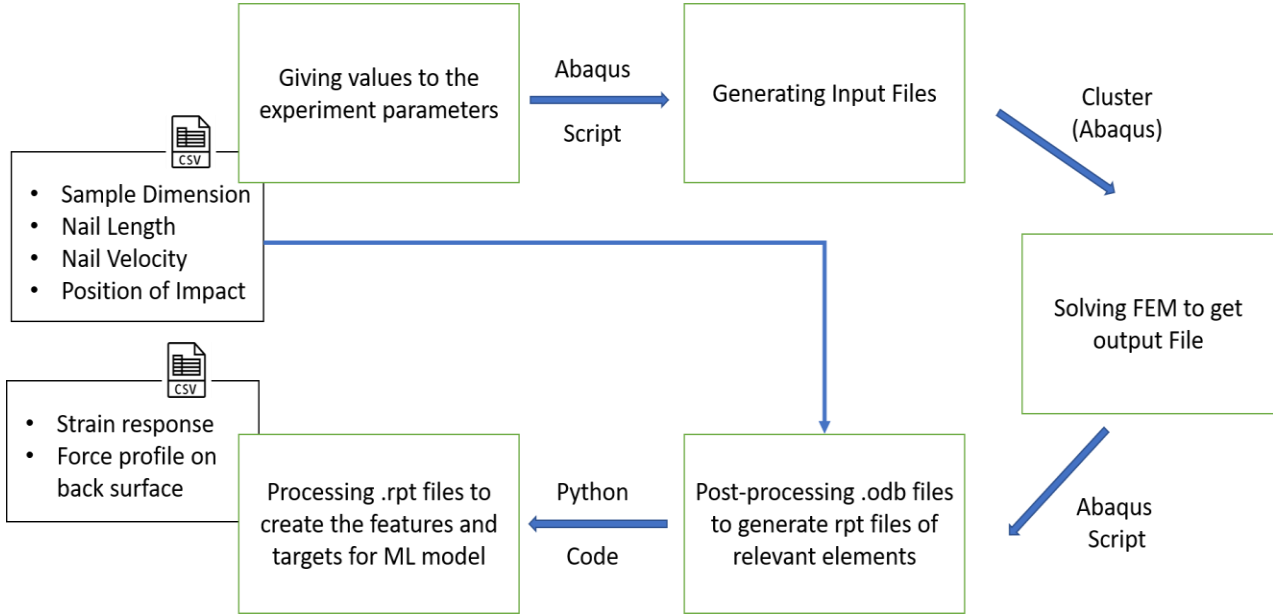


Figure 36. Flowchart for generating the low-fidelity dataset

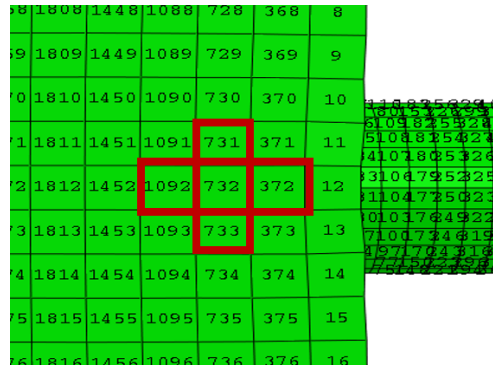


Figure 37. Elements considered for local response measurement while generating data

### 3.4.3 Low-Fidelity Model

LFM was implemented using the simulation dataset. The dataset had 1000 samples, out of which 800 were used for training the model and 200 for validation. The features and targets have a dimension of [1,201] each, corresponding to the uniform sampling done on load and strain profile throughout 20 micro-seconds. A fully connected NN was developed with 3 hidden layers of 400,

300, and 300 neurons, respectively. All the specifications of the NN are mention in Table 7. The activation function used here is leaky ReLU. Figure 38 shows the difference between ReLU and leaky ReLU activations. The choice was based on the type of output data which comprises both negative and positive values and is of much less magnitude than 1.

Table 7. Specifications of LFM

#Input dim. (Features)	201
#Output dim. (Target)	201
Training Samples	800
Validation Samples	200
Hidden Layers	[400, 300, 300]
Learning Rate	0.0015
Optimizer	Adam
Error Loss	MSE (Mean square error)
Epochs run	150

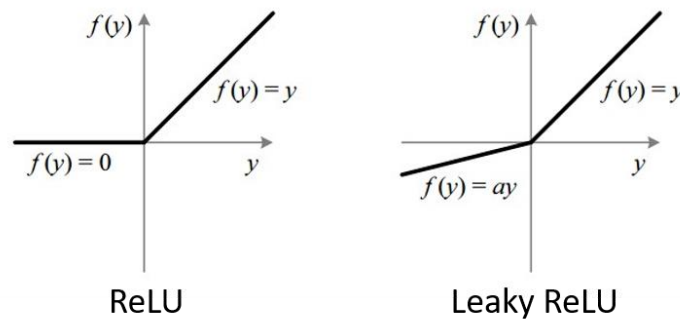


Figure 38. Activation function: ReLU v/s Leaky ReLU

The learning of the neural network can be observed in Figure 39. The loss function decreases with the number of epochs. We see that the validation loss also consistently decreases showing no overfitting. Figure 40 shows a few output samples and predicted values. The prediction gives very good results for our application.

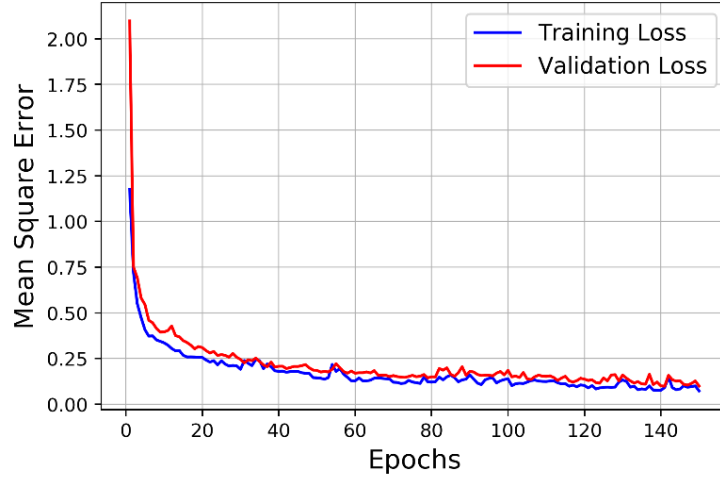


Figure 39. Loss curve for the low-fidelity model

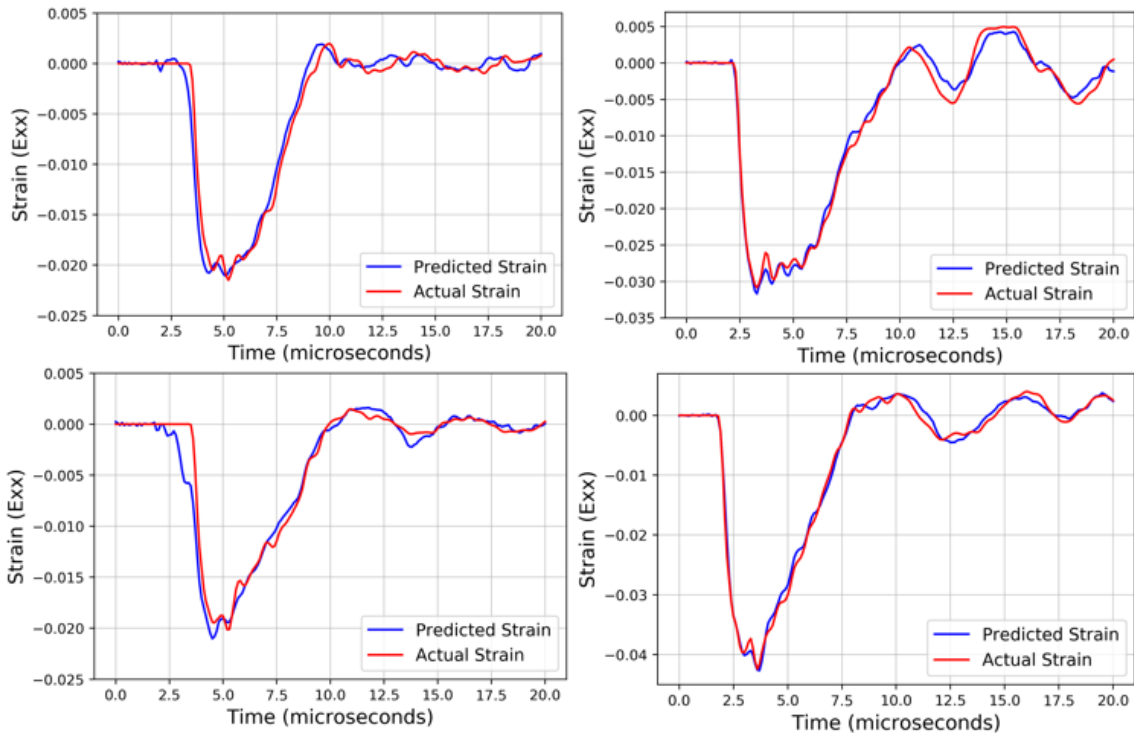


Figure 40. Sample predictions by the low-fidelity model

### 3.4.4 Multi-Fidelity Model

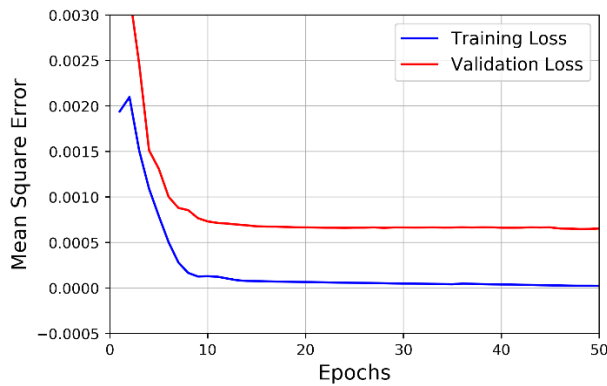
The NN architecture implemented for multi-fidelity modeling was the same as that of the toy model discussed above. The original input and output of the low-fidelity model (pre-trained with

low-fidelity data) were used as input features for the second neural network (NN2). This made the input dimension double as that of HFM. The specifications of NN2 for this model are present in

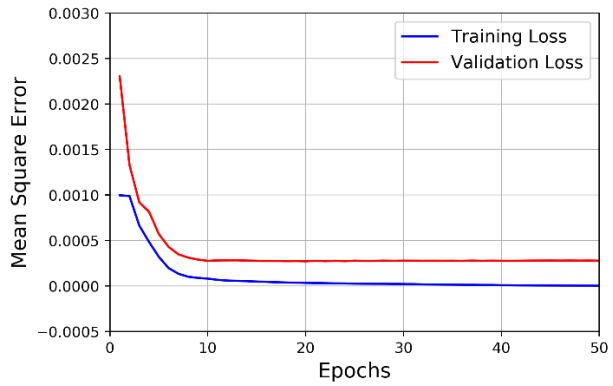
Table 8. A total of 30 samples were obtained from experiments, out of which 20 were used for training and 10 for validation. Figure 41 shows the training and validation curves of the multi-fidelity model and the high-fidelity model without any low-fidelity data.

Table 8. Specification for NN2 of MFM

#Input dim. (Features)	402
#Output dim. (Target)	21
Training Samples	20
Validation Samples	10
Hidden Layers	[500, 500, 150]
Learning Rate	0.0011
Optimizer	Adam
Error Loss	MSE (Mean square error)
Epochs run	50



(a)



(b)

Figure 41. Loss curves for (a) High-fidelity model (b) Multi-fidelity model

The multi-fidelity model much performs better than the high-fidelity model. The difference in the MSE loss between the two models is 0.0004, giving an average of 57.14% improvement in the



accuracy over the high-fidelity model. Figure 42 shows the comparison of predicted and actual strain for a few experiments. The prediction gives very good performance for lower strains and deviates a little from the original response at higher strains. A few deviations in the results were expected because of the sensitivity of the DIC and experimental error. Uncertainty quantification on the experiment could be done and those can be accounted for in the modeling via Gaussian process regression which was considered for future work in this study.

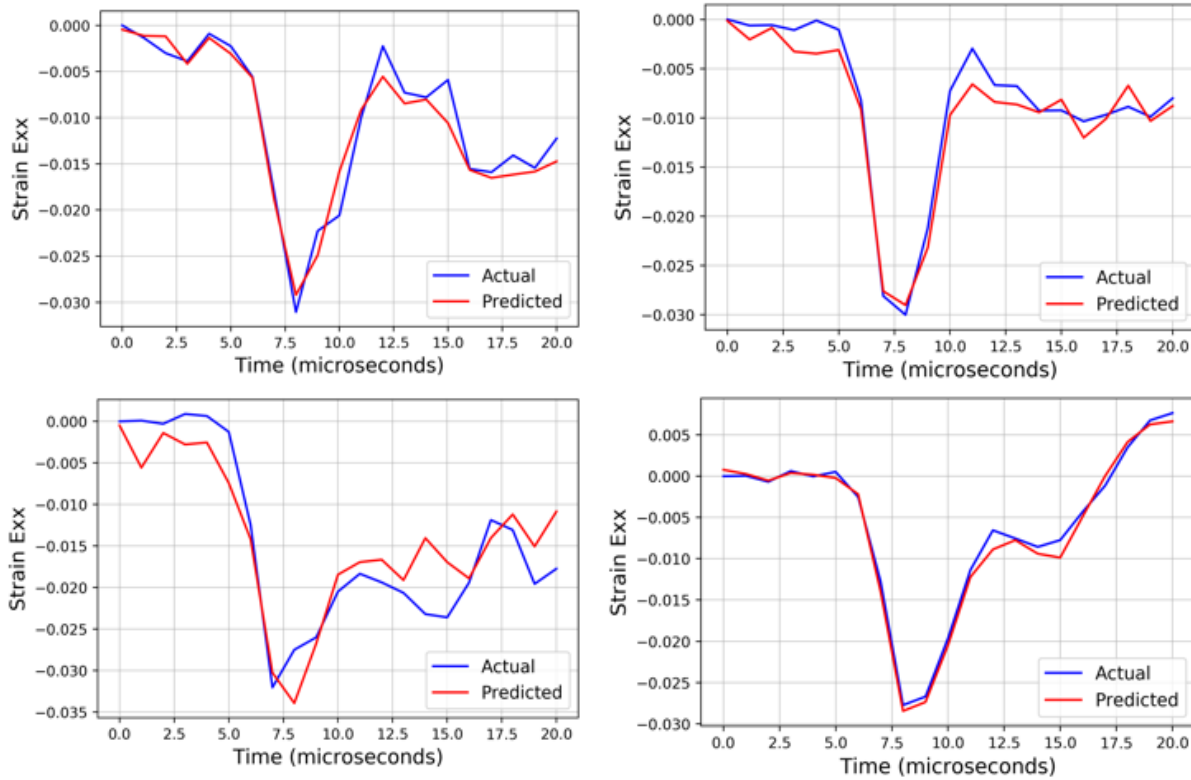


Figure 42. Measured v/s predict strain by MFM

### 3.5 Conclusion

During a flat nail impact on PMMA, localized compression was observed. This work aimed to predict the local response of a material using the load response observed at the back of the sample. The local response of the material was measured using DIC (Direct image correlation) to capture the deformation and strain spatially and temporally. The load response of the system was obtained using an FSR. The load response at low velocity followed the intuitive trend, but at higher

velocities, two peaks were observed. This behavior was attributed to the elastic-plastic response of the material under the impact point. The results from both the systems (DIC and sensors) were analyzed and compared with the simulation results. As the experiments are expensive and do not provide enough datasets for data-driven modeling, simulations were used to generate low-fidelity data. Multi-fidelity models leverage the existence of low-fidelity data in abundance and exploit the relationship between the low-fidelity and high-fidelity models. This relation was assumed to be much simpler than the original objective function that we want to find. MFM approach was implemented through neural networks to make the prediction. The MFM performed very well giving an average of 57.14% increase in performance over the high-fidelity model.

## 4. FUTURE WORK

The present approach provides a way to study the material response with a non-uniaxial experimental method and using data-driven modeling. As discussed in the introduction, the final aim is to use a half-space problem to predict the elastic-plastic properties of the material. The future work includes the following-

- To include sensor modeling and air pressure behind the nail in the simulations. As discussed in section 3.3.2, there was a significant difference observed in the load response between the sensor data and the simulation. This affects the quality of the low-fidelity data which affects the performance of the prediction. Modeling sensors and taking account of the air pressure can improve the prediction made by the multi-fidelity model with the same experimental data.
- To understand experimentally the dynamic elastic-plastic model for PMMA and weak shock wave propagation in half-space using the birefringence property of PMMA. This will also provide us with the mechanical properties of the material.
- To implement multi-fidelity modeling using the Gaussian process regression to consider and account for the uncertainty in the measurement of the experimental data.

## REFERENCES

- [1] "Experimental Techniques: Methods to Produce Dynamic Deformation," in *Dynamic Behavior of Materials*, 1994, pp. 296-322.
- [2] B. Hopkinson, "A method of measuring the pressure produced in the detonation of high explosives or by the impact of bullets," *Proceedings of the Royal Society of London. Series A, Containing Papers of a Mathematical and Physical Character*, vol. 89, no. 612, pp. 411-413, 1914, doi: doi:10.1098/rspa.1914.0008.
- [3] H. Kolsky, "An Investigation of the Mechanical Properties of Materials at very High Rates of Loading," *Proceedings of the Physical Society. Section B*, vol. 62, no. 11, pp. 676-700, 1949/11/01 1949, doi: 10.1088/0370-1301/62/11/302.
- [4] B. A. Gama , S. L. Lopatnikov , and J. W. Gillespie , Jr, "Hopkinson bar experimental technique: A critical review," *Applied Mechanics Reviews*, vol. 57, no. 4, pp. 223-250, 2004, doi: 10.1115/1.1704626.
- [5] T. V. Karman and P. Duwez, "The Propagation of Plastic Deformation in Solids," *Journal of Applied Physics*, vol. 21, no. 10, pp. 987-994, 1950, doi: 10.1063/1.1699544.
- [6] G. I. TAYLOR, "JAMES FORREST LECTURE 1946. THE TESTING OF MATERIALS AT HIGH RATES OF LOADING," *Journal of the Institution of Civil Engineers*, vol. 26, no. 8, pp. 486-519, 1946, doi: 10.1680/ijoti.1946.13699.
- [7] "Plastic Waves," in *Dynamic Behavior of Materials*, 1994, pp. 66-97.
- [8] J. Boussinesq, "Application des Potentiels," à l'Étude de l'Équilibre et du Mouvement des Solides Élastiques, Gauthiers-Villars, Paris, 1885.
- [9] P. Podio-Guidugli and A. Favata, "The Boussinesq Problem," in *Elasticity for Geotechnicians: A Modern Exposition of Kelvin, Boussinesq, Flamant, Cerruti, Melan, and Mindlin Problems*, P. Podio-Guidugli and A. Favata Eds. Cham: Springer International Publishing, 2014, pp. 79-114.
- [10] I. N. Sneddon, "The relation between load and penetration in the axisymmetric boussinesq problem for a punch of arbitrary profile," *International Journal of Engineering Science*, vol. 3, no. 1, pp. 47-57, 1965/05/01/ 1965, doi: [https://doi.org/10.1016/0020-7225\(65\)90019-4](https://doi.org/10.1016/0020-7225(65)90019-4).
- [11] L. Cheng, X. Xia, W. Yu, L. E. Scriven, and W. W. Gerberich, "Flat-punch indentation of viscoelastic material," *Journal of Polymer Science Part B: Polymer Physics*, vol. 38, no. 1, pp. 10-22, 2000, doi: 10.1002/(sici)1099-0488(20000101)38:1<10::Aid-polb2>3.0.Co;2-6.
- [12] Y. Cao, D. Ma, and D. Raabe, "The use of flat punch indentation to determine the viscoelastic properties in the time and frequency domains of a soft layer bonded to a rigid substrate," (in eng), *Acta Biomater*, vol. 5, no. 1, pp. 240-248, 2009/01// 2009, doi: 10.1016/j.actbio.2008.07.020.
- [13] W. Schepers, S. Savidis, and E. Kausel, "Dynamic stresses in an elastic half-space," *Soil Dynamics and Earthquake Engineering*, vol. 30, no. 9, pp. 833-843, 2010/09/01/ 2010, doi: <https://doi.org/10.1016/j.soildyn.2009.11.004>.
- [14] C. Vrettos, "Time-harmonic boussinesq problem for a continuously non-homogeneous soil," *Earthquake Engineering & Structural Dynamics*, vol. 20, no. 10, pp. 961-977, 1991, doi: 10.1002/eqe.4290201006.

- [15] D. M. Marsh and A. H. Cottrell, "Plastic flow in glass," *Proceedings of the Royal Society of London. Series A. Mathematical and Physical Sciences*, vol. 279, no. 1378, pp. 420-435, 1964/06/09 1964, doi: 10.1098/rspa.1964.0114.
- [16] W. Hirst and M. G. J. W. Howse, "The Indentation of Materials by Wedges," *Proceedings of the Royal Society of London. Series A, Mathematical and Physical Sciences*, vol. 311, no. 1506, pp. 429-444, 1969. [Online]. Available: <http://www.jstor.org/stable/2416241>.
- [17] K. L. Johnson, "The correlation of indentation experiments," *Journal of the Mechanics and Physics of Solids*, Article vol. 18, no. 2, pp. 115-126, 1970, doi: 10.1016/0022-5096(70)90029-3.
- [18] R. Hill, *The mathematical theory of plasticity*. Clarendon Press ; New York : Oxford University Press (in English), 1998.
- [19] R. Sobeski and G. Urgessa, "Review of Quasi-Analytical and Cavity Expansion Methods for Projectile Penetration of Concrete Targets," *International Journal of Protective Structures*, vol. 6, no. 1, pp. 43-64, 2015/03/01 2015, doi: 10.1260/2041-4196.6.1.43.
- [20] G. Ben-Dor, A. Dubinsky, and T. Elperin, "Analysis of ballistic properties of layered targets using cavity expansion model," (in English), *Int. j. fract*, vol. 90, no. 4, pp. L63-L67, 1998.
- [21] R. Masri and D. Durban, "Dynamic Spherical Cavity Expansion in an Elastoplastic Compressible Mises Solid," *Journal of Applied Mechanics*, vol. 72, no. 6, pp. 887-898, 2004, doi: 10.1115/1.1985428.
- [22] P. Chadwick, "THE QUASI-STATIC EXPANSION OF A SPHERICAL CAVITY IN METALS AND IDEAL SOILS," *The Quarterly Journal of Mechanics and Applied Mathematics*, vol. 12, no. 1, pp. 52-71, 1959, doi: 10.1093/qjmam/12.1.52.
- [23] H. G. Hopkins, "Dynamic Expansion of Spherical Cavities in Metal," *Progress in Solid Mechanics*, 1960.
- [24] R. F. Bishop, R. Hill, and N. F. Mott, "The theory of indentation and hardness tests," *Proceedings of the Physical Society*, vol. 57, no. 3, pp. 147-159, 1945/05/01 1945, doi: 10.1088/0959-5309/57/3/301.
- [25] E. L. McDowell, "Deviatoric Effects in High Intensity Stress Waves. Air Force Weapons Laboratory.," *Technical Report AFWL-TR-65-15*, 1965.
- [26] J. N. Goodier, "On the Mechanics of Indentation and Cratering in Solid Targets of Strain-Hardening Metal by Impact of Hard and Soft Spheres," *Proceedings of the 7th Symposium on Hypervelocity Impact III*. NY: AIAA, 1965.
- [27] U. Ali, K. J. B. A. Karim, and N. A. Buang, "A Review of the Properties and Applications of Poly (Methyl Methacrylate) (PMMA)," *Polymer Reviews*, vol. 55, no. 4, pp. 678-705, 2015/10/02 2015, doi: 10.1080/15583724.2015.1031377.
- [28] H. Hashim *et al.*, "Natural rubber-grafted with 30% poly(methylmethacrylate) characterization for application in lithium polymer battery," in *2010 International Conference on Science and Social Research (CSSR 2010)*, 5-7 Dec. 2010 2010, pp. 485-488, doi: 10.1109/CSSR.2010.5773825.
- [29] L.-H. Lee and W.-C. Chen, "High-Refractive-Index Thin Films Prepared from Trialkoxysilane-Capped Poly(methyl methacrylate)-Titania Materials," *Chemistry of Materials*, vol. 13, no. 3, pp. 1137-1142, 2001/03/01 2001, doi: 10.1021/cm000937z.
- [30] B. Adhikari and S. Majumdar, "Polymers in sensor applications," *Progress in Polymer Science*, vol. 29, no. 7, pp. 699-766, 2004/07/01/ 2004, doi: <https://doi.org/10.1016/j.progpolymsci.2004.03.002>.

- [31] N. McCormick and J. Lord, "Digital Image Correlation," *Materials Today*, vol. 13, no. 12, pp. 52-54, 2010/12/01/ 2010, doi: [https://doi.org/10.1016/S1369-7021\(10\)70235-2](https://doi.org/10.1016/S1369-7021(10)70235-2).
- [32] M. Sharafisafa, Z. Aliabadian, and L. Shen, "Crack initiation and failure development in bimrocks using digital image correlation under dynamic load," *Theoretical and Applied Fracture Mechanics*, Article vol. 109, 2020, Art no. 102688, doi: 10.1016/j.tafmec.2020.102688.
- [33] S. Hong *et al.*, "Interior fracture analysis of rubber-cement composites based on X-ray computed tomography and digital volume correlation," *Construction and Building Materials*, Article vol. 259, 2020, Art no. 119833, doi: 10.1016/j.conbuildmat.2020.119833.
- [34] N. Hedayati and R. Hashemi, "Some practical aspects of digital image correlation technique to evaluate anisotropy coefficient and its comparison with traditional method," *Journal of Testing and Evaluation*, Article vol. 48, no. 6, 2020, Art no. Jte20180227, doi: 10.1520/JTE20180227.
- [35] E. B. Dolan, S. W. Verbruggen, and R. A. Rolfe, "Chapter 1 - Techniques for studying mechanobiology," in *Mechanobiology in Health and Disease*, S. W. Verbruggen Ed.: Academic Press, 2018, pp. 1-53.
- [36] D. E. Grady, "Dynamic properties of ceramic materials," United States, 1995. [Online]. Available: [http://inis.iaea.org/search/search.aspx?orig\\_q=RN:26069379](http://inis.iaea.org/search/search.aspx?orig_q=RN:26069379)
- [37] T. Kojo, A. Tagaya, and Y. Koike, "Mechanism of generation of birefringence in poly(methyl methacrylate/styrene)," *Polymer Journal*, vol. 44, no. 2, pp. 167-173, 2012/02/01 2012, doi: 10.1038/pj.2011.101.
- [38] S. Raha and P. B. Bowden, "Birefringence of plastically deformed poly(methyl methacrylate)," *Polymer*, vol. 13, no. 4, pp. 174-183, 1972/04/01/ 1972, doi: [https://doi.org/10.1016/0032-3861\(72\)90042-0](https://doi.org/10.1016/0032-3861(72)90042-0).
- [39] B. E. Read, "Dynamic birefringence of poly(methyl methacrylate)," *Journal of Polymer Science Part C: Polymer Symposia*, vol. 16, no. 4, pp. 1887-1902, 1967, doi: 10.1002/polc.5070160405.
- [40] N. Tarjányi, D. Káčik, M. Uhrčík, and P. Palček, *PMMA birefringence-based optical sensor of load* (SPIE Photonics Europe). SPIE, 2020.
- [41] B. Koohbor, A. Kidane, M. A. Sutton, X. Zhao, and S. Mallon, "Analysis of dynamic bending test using ultra high speed DIC and the virtual fields method," *International Journal of Impact Engineering*, vol. 110, pp. 299-310, 2017/12/01/ 2017, doi: <https://doi.org/10.1016/j.ijimpeng.2016.12.021>.
- [42] S. Choi, J. J. Alonso, I. M. Kroo, and M. Wintzer, "Multifidelity Design Optimization of Low-Boom Supersonic Jets," *Journal of Aircraft*, vol. 45, no. 1, pp. 106-118, 2008, doi: 10.2514/1.28948.
- [43] K. J. Chang, R. T. Haftka, G. L. Giles, and P.-J. Kao, "Sensitivity-based scaling for approximating structural response," *Journal of Aircraft*, vol. 30, no. 2, pp. 283-288, 1993, doi: 10.2514/3.48278.
- [44] R. Vitali, R. T. Haftka, and B. V. Sankar, "Multi-fidelity design of stiffened composite panel with a crack," *Structural and Multidisciplinary Optimization*, vol. 23, no. 5, pp. 347-356, 2002/06/01 2002, doi: 10.1007/s00158-002-0195-1.
- [45] M. Eldred, "Recent Advances in Non-Intrusive Polynomial Chaos and Stochastic Collocation Methods for Uncertainty Analysis and Design," in *50th AIAA/ASME/ASCE/AHS/ASC Structures, Structural Dynamics, and Materials Conference*.

- [46] A. S. Padron, J. J. Alonso, and M. S. Eldred, "Multi-fidelity Methods in Aerodynamic Robust Optimization," in *18th AIAA Non-Deterministic Approaches Conference*.
- [47] A. I. J. Forrester, A. Sóbester, and A. J. Keane, "Multi-fidelity optimization via surrogate modelling," *Proceedings of the Royal Society A: Mathematical, Physical and Engineering Sciences*, vol. 463, no. 2088, pp. 3251-3269, 2007, doi: doi:10.1098/rspa.2007.1900.
- [48] M. Raissi, P. Perdikaris, and G. E. Karniadakis, "Inferring solutions of differential equations using noisy multi-fidelity data," *Journal of Computational Physics*, vol. 335, pp. 736-746, 2017/04/15/ 2017, doi: <https://doi.org/10.1016/j.jcp.2017.01.060>.
- [49] P. Perdikaris, M. Raissi, A. Damianou, N. D. Lawrence, and G. E. Karniadakis, "Nonlinear information fusion algorithms for data-efficient multi-fidelity modelling," *Proceedings of the Royal Society A: Mathematical, Physical and Engineering Sciences*, vol. 473, no. 2198, p. 20160751, 2017, doi: doi:10.1098/rspa.2016.0751.
- [50] J. Laurenceau and P. Sagaut, "Building Efficient Response Surfaces of Aerodynamic Functions with Kriging and Cokriging," *AIAA Journal*, vol. 46, no. 2, pp. 498-507, 2008, doi: 10.2514/1.32308.
- [51] E. Minisci and M. Vasile, "Robust Design of a Reentry Unmanned Space Vehicle by Multifidelity Evolution Control," *AIAA Journal*, vol. 51, no. 6, pp. 1284-1295, 2013, doi: 10.2514/1.J051573.
- [52] M. Raissi, P. Perdikaris, and G. E. Karniadakis, "Physics-informed neural networks: A deep learning framework for solving forward and inverse problems involving nonlinear partial differential equations," *Journal of Computational Physics*, vol. 378, pp. 686-707, 2019/02/01/ 2019, doi: <https://doi.org/10.1016/j.jcp.2018.10.045>.
- [53] X. Meng and G. E. Karniadakis, "A composite neural network that learns from multi-fidelity data: Application to function approximation and inverse PDE problems," *Journal of Computational Physics*, vol. 401, p. 109020, 2020/01/15/ 2020, doi: <https://doi.org/10.1016/j.jcp.2019.109020>.